Faculty of Transportation Engineering and Vehicle Engineering
Budapest University of Technology and Economics
Department of Control for Transportation and Vehicle Systems

CORRECTION OF AIRSPEED SENSOR ERROR WITH SPEED ESTIMATION ALGORITHMS

Scientific Student Conference Thesis

Tamás Baár
Bence Béke

Consultant:
Dr. Péter Bauer

October 27, 2015

Abstract

In order to achieve safe flight conditions, it is crucial to keep the airspeed between allowable limits. If the airspeed drops drastically the airplane will stall which can lead to fatal accidents, as it happened in the case of Air France 447 in 2009. When airspeed increases beyond an upper limit, the aerodynamic stresses may cause serious damages to the wing and/or fuselage, and lead to the loss of the airplane (An-148 accident in 2011).

Onboard an airplane usually multiple sensors (or multiple sensor systems) measure the airspeed, but unfortunately as the above mentioned examples show sometimes it is not enough. One possible solution can be an estimator algorithm which relies on other sensor measurements, and works completely independent of airspeed sensors. The MTA SZTAKI develops such an algorithm in the frame of the RECONFIGURE EU FP7 project. We are involved to the development of the mentioned algorithm. The results are validated on the linear and non-linear simulation models of a real Airbus A380 airplane provided by Airbus.

The estimation procedure is based on the Multiple Model Adaptive Estimation (MMAE) concept. Kalman Filters (KFs) are developed to linearized models at different airspeeds. They estimate the system′s states through acceleration and GPS measurements. The filter residuals are composed as the difference between the predicted system outputs and the real measured outputs. The filter which belongs to the lowest residual value is the one which works closest to the actual flight conditions, and this provides the estimate of the airspeed of the airplane.

The MMAE methods found in the corresponding literature provide a staircase function as estimated airspeed even if airspeed changes continuously, because they always choose the parameter of that Kalman Filter which works closest to the actual conditions. In order to have a smooth estimation it is necessary to use numerous models which are linearized at different speeds. To overcome this problem we introduced a new solution method, which interpolates between the estimated values, and provides a smooth estimation with minimal extra calculations. This made possible the use of less models, and we could cover the whole flight envelope of an A380 airplane with only 5 Kalman Filters.

The developed estimators use GPS speed measurements, which in the presence of wind disturbance differ from the airspeed exactly with the wind speed value. In order to estimate correct airspeed values, we also had to estimate the wind speed with reformulated filters. In this case inside the state and disturbance estimator KF banks we had to define multiple models based on the airplane weight and airspeed. This led to a total number of 5x5 linearized models necessary to cover the flight envelope.

The developed algorithms were successfully tested on the Airbus A380 linear and non-linear simulation models. Final validation will be carried out by project partners during autumn.

Contents

List of abbreviations

A/C: Aircraft
AOA: Angle of Attack
CAS: Calibrated Airspeed
CG: Center of Gravity
EAS: Equivalent Airspeed
FCS: Flight Control System
FL: Flight Level
FTC: Fault Tolerant Control
GPS: Global Positioning System
IAS: Indicated Air Speed
ISP: Integrated Static Port
KF: Kalman Filter
LPV: Linear Parameter-Varying control
LTI: Linear Time Invariant control
MFP: Multi Functional Probe
MMAE: Multiple Model Adaptive Estimation
PPE: Posterior Probability Estimator
SSA: Sideslip Angle
SVD: Singular Value Decomposition
TAS: True Airspeed

Chapter 1

Introduction

1.1 The role of airspeed in aviation

1.1.1 The importance of airspeed

The correct knowledge of airspeed has a great importance in aerodynamics and also in flight safety. The airplanes are raised from the ground by the so called lift force generated on their wings, which is a function of the velocity relative to the air. Once the flight parameters are known, the lift force can be calculated as

$$L = \frac{1}{2}\rho V^2 S C_L \tag{1.1}$$

where ρ is the air density, V is the speed relative to air, S is the wing area, and C_L is the lift coefficient at the current operating condition. From equation (1.1) it can be easily seen that the lift force is strongly coupled on airspeed. In order to keep the airplane in the air, it is necessary to achieve a minimum flying speed when the lift force generated on the wing equals to the weight of the aircraft. However for safe flight conditions it is not enough to keep the airspeed over the minimum flying speed, it is also important to keep the speed below the maximum allowable limit. When an airplane is maneuvering aerodynamic forces and moments are rising on the body and the control surfaces. These forces and moments similarly to the lift force are also a function of the airspeed, and increasing quadratically by the increase of speed. All aircraft structures have an upper limit, which describes the maximum value of stresses they are capable to survive. These limits are characterized by the load factor. The load factor can be defined as:

$$n = \frac{L}{W} = \frac{C_{Lmax}\frac{\rho V^2}{2}S}{W} = \frac{V^2}{\frac{2W}{C_{Lmax}\rho S}} = \left(\frac{V}{V_S}\right)^2 \tag{1.2}$$

Where W is the weight of the aircraft, and V_S is the stall speed. Equation (1.2) tells that if the airspeed increases, the load on the aircraft also increases. The airworthiness regulations give the maximum value of n for different aircraft types. In the case of airliners this value ranges from 2.5 to 3.8. Figure (1.1) shows the general form of a V-n flight envelope, where the maximum allowable load factor is plotted as a function of airspeed. During operation the aircraft has to stay inside the green zone. On the diagram the following speeds are mentioned: V_S stall speed, V_A stall speed under peak maneuver load, V_C design cruise speed, V_D limiting dive speed. V_D also stands for the maximum allowable speed, at a speed beyond this limit the resulting aerodynamic forces may cause significant damage on the structure. For further details

on the flight envelope diagram the reader is invited to consult [1]. More information about the resulting aerodynamic forces or moments can be found in [2].

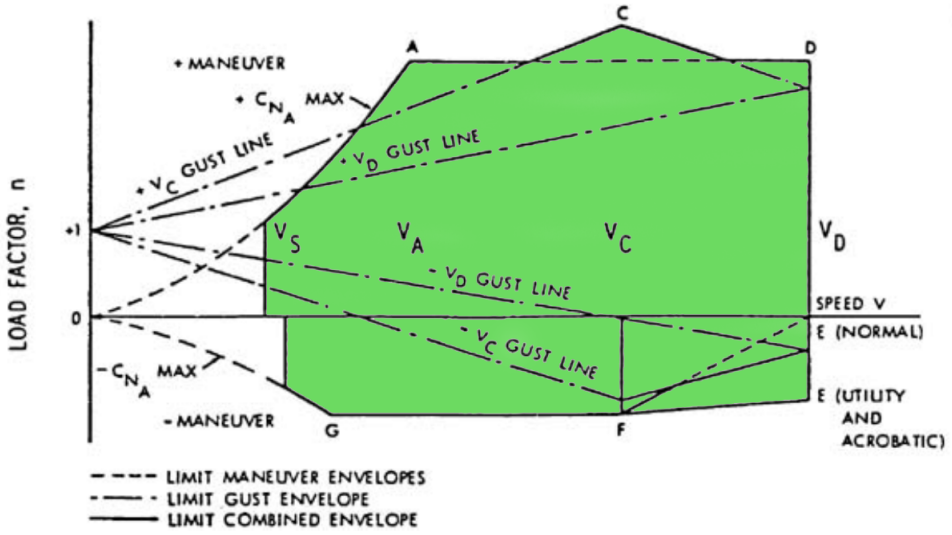

Figure 1.1: General form of V-n flight envelope diagram [1]

1.1.2 The measurement and definitions of airspeed

Onboard an aircraft (A/C) airspeed is measured based on the difference of the stagnation pressure and the static pressure around the airplane. The stagnation pressure (or ram air pressure, total pressure) is measured by a Pitot tube. The static pressure is measured by static pressure ports on the aircraft fuselage. The airspeed is basically calculated based on the Bernoulli equation:

$$p_t = p_s + \rho \frac{V^2}{2} \tag{1.3}$$

$$V^2 = \frac{2(p_t - p_s)}{\rho} \tag{1.4}$$

where p_t and p_s are the total and static pressures respectively.

Airspeed definitions

In aeronautics multiple airspeeds are defined [3, 4].

- **Indicated airspeed - IAS**

  Indicated airspeed is a speed shown by the airspeed indicator. The airspeed sensor system calculates the difference between the ram air pressure and static pressure. This pressure difference in the indicator gauge is then converted to airspeed by applying a suitable scaling.

- **Calibrated airspeed - CAS (or Vcas)**

  The IAS does not represent the correct airspeed, because it is corrupted by various errors. The calibrated airspeed is the indicated airspeed corrected for instrument, position and installation errors. Position errors are due to the position of the static pressure sensors. The airplane's body interacts with the flow around it, and modifies the flow parameters such as the pressure field in the neighborhood of the airplane. This means that the static pressure sensor measures a different pressure value than it is in the free stream. The Pitot tube is also affected by the stream modification effect of the body, that is the reason why designers try to place it far from the fuselage.

- **Equivalent airspeed - EAS**

  The equivalent airspeed is a speed at sea level which produces the same incompressible dynamic pressure as the true airspeed at the altitude which the airplane is flying.

- **True airspeed - TAS**

  True airspeed is the speed of the aircraft relative to the surrounding air. In case the speed relative to the ground (V_g), and the wind speed (V_w) are known it can be calculated as

$$V_t = V_g - V_w \tag{1.5}$$

- **Groundspeed**

  Groundspeed is the speed of the aircraft relative to the ground. This speed can be measured through GPS measurements or by a ground-based radar.

1.1.3 Possible failures in airspeed sensor system

In aviation history most of the accidents due to the loss of reliable airspeed data are happened because of a blockage in the airspeed sensor's pipe system. The most probable cause of such a blockage is ice formation, but other reasons can be considered as well. In the forthcoming, numerous examples are presented when corrupted airspeed sensor data led to hazardous situations or even aircraft loss.

Austral Líneas Aéreas Flight 2553

On the 10th of October 1997 Austral Líneas Aéreas Flight 2553 impacted into the ground with 74 people onboard. The accident is still considered as the most serious one in Uruguay's aviation history. The airplane was a McDonell Dougles DC-9 and took off from Posadas. During the flight they encountered bad weather conditions, with Cumulonimbus clouds and outside temperature of -59 deg. Celsius. The airspeed indicator fell to a low indicated airspeed due to ice formation on the Pitot tube, which reduced the amount of air entering the sensor. The pilots believed they are flying around the stall speed, and they lowered the wing slats to increase lift. Actually the airplane was flying at a speed even higher than the normal, close to the never exceed speed limit when the aerodynamic forces can cause structural damage. As the slats were lowered at a speed much above their operational limit, one of them was torn from the aircraft causing asymmetry between the two wings, which led to an uncontrollable flight and the loss of the airplane [5].

Aeroperú Flight 603

Aeroperú Flight 603 was a flight around midnight from Lima airport on the 2nd of October, 1996. The airplane involved to the accident was a Boeing 757. Shortly after take off pilots discovered that the flight instruments are not working correctly, and the onboard computer is giving false errors such as rudder ratio, overspeed, underspeed, and flying too low. They decided to return to the airport. Without reliable flight instruments and with continuous contradictionary warnings they believed that they are on a safe altitude. Without the ability to monitor the airspeed they experienced multiple stalls, which led to the loss of altitude without a reliable sign on the altimeter which showed an altitude much higher than it really was. The airplane crashed into the water. The investigations found out that the cause of the failure was a maintenance worker's failure who did not remove the tape cover from the airplane's static pressure sensing slots after the cleaning of the fuselage [6].

Birgenair Flight 301

The aircraft took off from Puerto Plata's international airport on the 6th of February, 1996. The airplane was a Boeing 757-225. During take off the captain recognized that his airspeed indicator is not working correctly, but the first officer's one was functional. He decided to take off. While the airplane was climbing, the captain's indicator showed 350 knots. The autopilot was fed with speed information from the captain′s equipment, and so it increased the pitch-up attitude of the airplane and decreased the power, in order to lower the airspeed. Actually the plane was flying much slower, and the autopilot's intervention caused a stall of the airplane. Since the co-pilot's equipment was functioning well, the airplane gave contradictory warnings as flying too fast or too slow. They could not recover the plane from the stall. The investigations concluded that one of the three Pitot tubes onboard the airplane was malfunctioning. The

aircraft had not flown in 20 days before the accident, and in part of this time the tubes were uncovered. The investigators suppose that this time was enough for a wasp to block the Pitot tube by a net [7].

Antonov An-148 crash

On the 5th of March 2011, an An-148 crashed 560 kms south from Moscow. The aircraft was destroyed in the accident. Witnesses of the accident said that a wing was separated from the aircraft while it was in the air, and wrecks were recovered from two separate locations. The examination of the flight recorder data showed that one airspeed indicator was failed, and showed much lower speed than the real one. The pilots increased the speed of the airplane, and so exceeded the never exceed speed of the plane. The aerodynamic forces torn the airplane apart [8].

Air France Flight 447

On the 1st of June 2009, an Airbus A330-203 took up from Rio de Janeiro and headed to Paris. After two hours of flight the airplane was lost over the Atlantic Ocean. Analysis of weather conditions pointed out it is possible that in the last 12 minutes the airplane was flying through highly turbulent air and thunderstorm. These flight conditions may caused icing on the pressure sensors. The plane was stalled, and the pilots could not restore the flight envelope. The investigators pointed out that a series of mistakes from the misunderstanding of the situation led to the loss of the airplane [9].

The U.S. National Transportation Safety Board (NTSB) reported two similar failures involving Airbus A330s as Air France 447 had. On the 21st of May 2009, TAM Airlines Flight 8091 was flying from Miami to Sao Paolo when during cruise flight they lost the primary speed and altitude data. The crew used backup sensors, and the primary data was restored after five minutes. The plane landed in Sao Paulo without any injuries or damage. On the 23rd of June 2009, a Northwest Airlines A330 experienced same primary flight data outage during cruising from Hong Kong to Tokyo. The plane encountered an intense rain and both the captain's and co-pilot's indicators showed a huge decrease in the plane's airspeed. The outage lasted for more than three minutes, but they maintained airspeed and flew the most direct route out of the storm. Nobody was injured. Australian investigators reported two similar incidents with a Jetstar Airbus A330. The outage only lasted in both cases for a few seconds, and was due to an obstruction in one of the Pitot tubes. All of the events happened with environmental conditions outside of the specified certification requirements [10].

After 2001 Airbus A330s were equipped with Goodrich [0851HL] or Thales [C16195QAA] probes, however Thales "AA" probes have been found to be more susceptible to high-altitude icing. The European Aviation Safety Agency (EASA) and the U.S. Federal Aviation Administration (FAA) in August 2009 issued airworthiness directives for the replacements of all Thales "AA" probes on Airbus A330s and A340s. They required Goodrich [0851HL] probes at captain's and standby positions, and [0851HL] or Thales [C16195BA] probe on the first officer's position. In 2009 EASA also proposed an airworthiness directive that require A330/340 Flight Control Computer (FCC) software modification to avoid re-engagement of autoflight systems with corrupted airspeed data [11].

1.2 The Reconfigure project

As the above mentioned examples demonstrate, sometimes even the double or triple systems are not enough to prevent a catastrophe. That is the reason why the European Commission founded the Reconfigure (Reconfiguration of Control in Flight for Integral Global Upset Recovery) program under the name Reconfigure EU FP7. This project is a joint research between several European technical institutions, with the aim of developing future technical solutions which can provide increased air safety. Today′s airliners are based on a fault tolerant fail-safe design approach and use control laws in their Flight Control Systems which lose functionality depending on the nature of the system, sensor or actuator failure. Future need urge the development of solutions which provide all-time all-event availability of control and guidance functions as long as it possible. In the frame of the Reconfigure researchers investigated sensor and actuator fault scenarios, and proposed methods for system reconfiguration maintaining the same flight performance. [12].

The vast majority of modern airliners are controlled by Fly-by-Wire systems. The aircraft's flight control computers send electronic signals to operate the control surfaces or engine controls, and provide to the pilot performance information. The system supervises the pilot's movements, and prevents dangerous maneuvers which could place the aircraft outside the desired flight envelope. These systems are based on control laws (or control modes) and provide Fly-by-Wire protections and control enhancement. The control mode is selected based on the phase of the flight and the experienced sensor, system or actuator faults. Depending on the nature of the failure the applicable control laws may vary from fully functional and protected through partly functional (regarding to the failure type) to fully unprotected and unfunctional operation. For instance in the case of an Airbus A340 airplane the following control laws and provided protections are available [13, 14]:

- **Normal Law:**
  The aim of Normal Mode is to provide a stable and maneuverable flight inside the flight envelope limits (regardless of airspeed, altitude, gross weight or Center of Gravity). It is the most commonly used, and able to handle single failures. It contains Pitch and Bank angle control, Auto Trim, and it provides five different protections in order to avoid overcontrolling or overstressing the aircraft. The available protections are High Angle of Attack, Load Factor, High Pitch Attitude, Bank Angle and High Speed protections.

- **Alternate Law:**
  This is the first reconfiguration mode of the Fly-by-Wire system. In case of double failures for example double hydraulic failure, the redundancy of the used equipments is not enough to achieve Normal Law, and it's protections. Alternate Law is triggered. During landing Alternate Law changes to direct law at 100 ft RA. The autopilot availability is depending on the type of the failure. The available protections change as follows. High Angle of Attack protection replaced by Stall Warning at 1.03 VS1g (stall speed at 1 g). Load Factor and Bank Angle protections are maintained. The Pitch Attitude protection is lost, and the High Speed protection is replaced by Overspeed Warning.

- **Direct Law:**
  In case of Direct Law autopilot and auto-trim are not available, and also all protections

are lost, but aural overspeed and stall warnings remain. Yaw Damper is still available to provide a minimal turn coordination.

- **Mechanical backup system:**
  The purpose of this system is to allow the pilots to control the aircraft after a total loss of electronics, flight computers, elevators ailerons and spoilers. It allows the crew to stabilize the flight path, while recovering a control law from the above mentioned ones. It is not designed for flying an approach or landing.

Current airliners use the same or similar fault tolerant control (FTC) strategies in their flight control systems (FCS), which are based on fail-safe approaches, where in case of failure the normal control mode switches to a more robust alternate law, or even to a direct mode if necessary. Moving from normal towards direct law, the level of stability provided by the system reduces, however the advantages of this approach are the ease of design, analysis and certification.

The control laws are designed off-line, for different levels of robustness, and each includes guidance and control functions which assist the pilot during the flight. As the control law changes from normal to direct, the piloting work becomes harder and harder, and as the functions become deactivated (Direct Law), the autopilot and other systems are completely unavailable.

It seems that the design paradigm at aircraft manufacturers is changing from the above mentioned robust stability towards a performance oriented one, which provides full-time and all-event availability of performance optimized control and guidance functions. This means control and guidance functions with extended operability range.

The main goal of RECONFIGURE is to investigate and develop aircraft guidance and control technologies that facilitate the automated handling of off-nominal/ abnormal events and optimize the aircraft status and flight. The automatism of the control and guidance will help alleviate the pilot's task and optimize performance by automatically reconfiguring the aircraft to its optimal flight condition [12].

In the frame of the project failure cases such as the loss of various airspeed sensors, or actuators connected to control surfaces were evaluated and solutions were proposed considering the world's largest airliner the Airbus A380.

Our work was to develop a solution for airspeed estimation in the case when airspeed sensors are partly or completely lost. We applied a Kalman Filter bank based on the Multiple Model Adaptive Estimation (MMAE) theory. Each KF inside the bank is operating at a linearized trim-point of the system describing the real airplane. With the aid of a Posterior Probability Evaluator the KF working closest to the actual operating point is selected based on the values of the filter residuals. It is proven that this filter provides the best estimate of the actual airspeed. Because of the nature of the MMAE algorithm this solution provided a staircase function, and the resolution was not accurate enough. We further developed the algorithm to provide a smoother result. After finishing this development we included the effect of wind disturbances and the variations in aircraft weight, flying altitude, CG positions. During the test campaign we experienced long time divergence of the filters, which was solved by numerical stabilization of the calculations.

The smoothing technique is presented in Chapter 2, while wind disturbance is considered in Chapter 3.

1.3 The Airbus A380

The presented algorithms were developed for the Airbus A380 aircraft, but they can be easily transferred to other airplanes as well. Before we go further into the details of the algorithms it is necessary to have an overview of the airplane.

The idea about building a competitor to the Boeing 747 was born at Airbus in 1988. In 1994 Airbus announced that they start the development of a very large airplane with a code name A3XX. After several years of development the A380 completed it's first flight in April 27, 2005, and entered to service in 2007 with Singapore Airlines [15] .

The plane has a 73 m length and an almost 80 m wingspan with a wing area of 845 square meters. The maximum take-off weight for the A380-800 is 560 tons, payload of 84 tons. Power plants are supplied by Engine Alliance and Rolls-Royce and ranging from 311 to 374 kN of thrust [16] .

After being airborne a group of several control surfaces provides smooth control of the airplane. Figure 1.2 shows these surfaces. The droops and slats are high-lift devices, and their function is to alter the wing camber and so reduce stalling speed. Flaps are also high-lift devices mounted on the trailing edges. Spoilers are devices to reduce lift over the wing. When extended, they reduce lift, and create drag. Ailerons are used for roll control about the plane's longitudinal axis. The rudders are for yaw control about the vertical axis. The aircraft's pitch, and so angle of attack can be controlled by elevators. The A380 is also equipped with two Trimmable Horizontal Stabilizers.

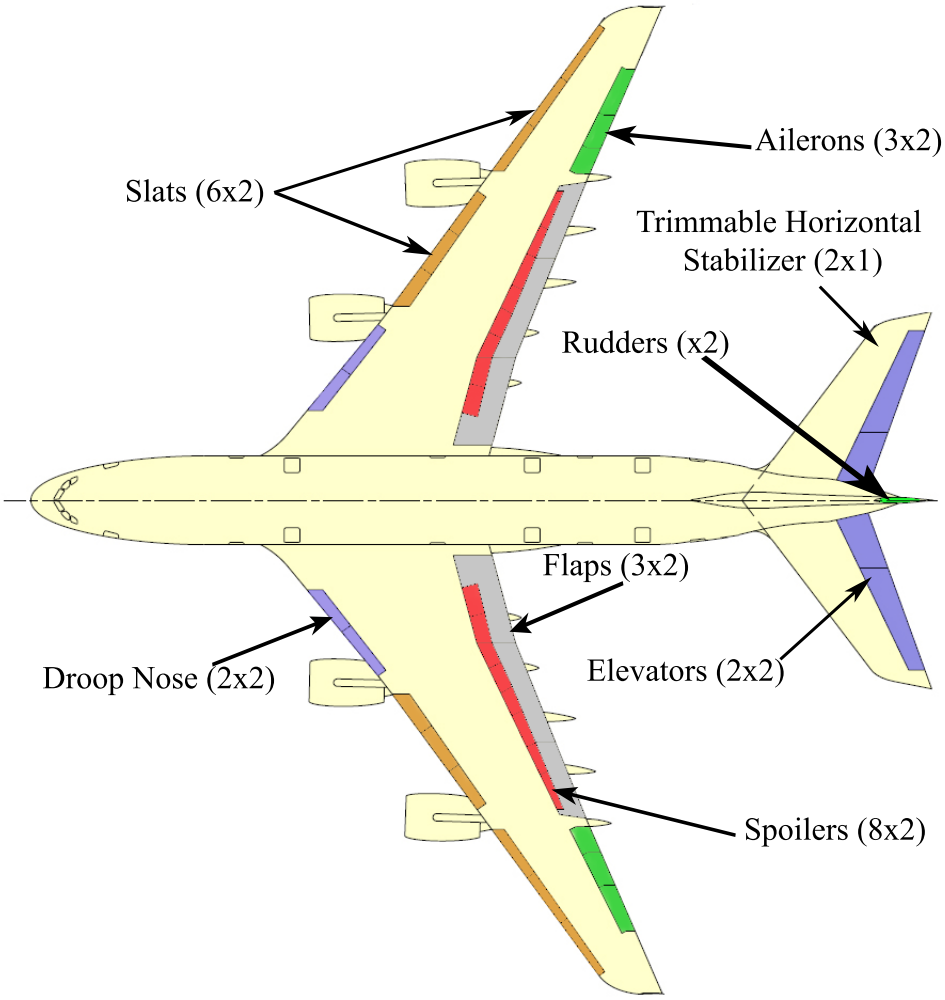

Figure 1.2: Control surfaces on an A380 [17]

The Airbus A380 is using several sensor ports for the flight conditions measurements. Figure 1.3 shows a schematics of an A380 with antennas and probe locations.

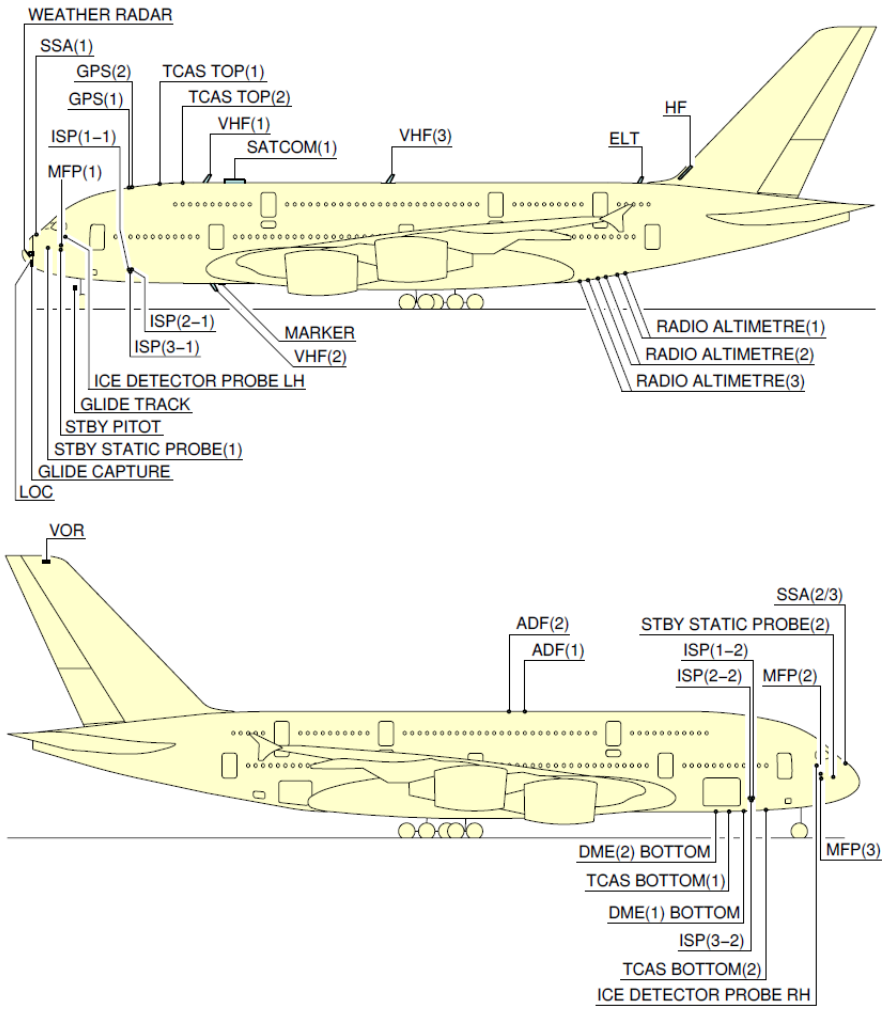

Figure 1.3: Antennas and Probe locations on an A380 [17]

Here SSA stands for Side Slip Angle measurement tools. MFP means Multi Functional Probe (for Pitot tube, Angle of Attack and Total Air Temperature measurements), and ISP is Integrated Static Port. Since we have seen the importance of icing around the Pitot tubes it is also important to mention the ice detectors on both sides of the airplane, and the two GPS receivers on the top of the plane since their measurements are used in the developed algorithms. The rest of the notations are not relevant in the present study. For further details see [17].

In the next chapter we start the description of our developments.

Chapter 2

Airspeed estimation in the absence of wind

Until now, we have presented the role of airspeed in aviation, and also showed demonstrating examples for the importance of correct airspeed information in all phases of flight, and we also discussed briefly the Airbus A380 which is the target of the development. In the forthcomings we present our solution for airspeed estimation what is based on Multiple Model Adaptive Estimation, and will be discussed in Section 2.1. For the design and evaluation process Airbus provided linear and non-linear models of A380 [18]. The linear model set contains system models in case of different altitudes, airspeed, aircraft weight and center of gravity positions. The altitude ranges from 5.000 feet to 35.000 feet with 7.500 feet steps. The provided airspeed, aircraft weight values and center of gravity positions are [210 240 270 300 335 (305)] (knots), [260 320 375 405 410 550 560] (tons) and [28 36 43] (%) respectively. The maximum airspeed is generally 335 knots at all altitudes, but for the 35.000 feet one the airspeed is restricted to 305 knots. Models selected from the linear model set are used for the MMAE design.

The design goal is to achieve a correct fault detection and Calibrated airspeed (CAS) estimation when the onboard CAS measurements are corrupted. From this two only CAS estimation is detailed in this work. As we mentioned before, CAS is measured by the Multi Functional Probes placed on both sides of the airplane. Since the Angle of Attack (AOA) is also measured by these probes, in case of a failure in CAS measurements the AOA and other air data measurement based information is also considered as lost. In this case the inertial measurements and GPS data (V_{SOL}) are still available. Measurement noises are generally not considered because a few tests proved that they do not have much impact on the results.

In the current chapter we assume no wind disturbance ($V_{SOL} = V_{AIR} = TAS$), and the design models were selected with an aircraft weight 410 tons and with a center of gravity (CG) at the position of 43% of the chord length.

In the models we consider the following states, measurements, and control inputs respectively.

$$x = \begin{bmatrix} Q1 \\ VSOL \\ ASOL \\ TETA \end{bmatrix} \quad y = \begin{bmatrix} NX1 \\ NZ1 \\ Q1 \\ \overline{VCAS} \\ TETA \end{bmatrix} \quad u = \begin{bmatrix} \delta_{e(LI)} \\ \delta_{e(RI)} \\ \delta_{e(LO)} \\ \delta_{e(RO)} \\ \delta_{THS} \end{bmatrix} \tag{2.1}$$

Where x contains the Pitch rate (Q1), the Ground Speed (V_{SOL}), the Angle of Attack (A_{SOL})respect

to the ground, and the Pitch angle (THETA). The measurement vector is built up from the measurement data of the x and z directional acceleration sensors, the Pitch rate, the calculated CAS, and the Pitch angle. The u vector contains the Left Inboard, Right Inboard, Left Outboard, Right Outboard Elevator and the Trimmable Horizontal Stabilizer deflections respectively. The latter only contribute to the slow dynamics and so it's effect was neglected in the final model. As mentioned before without wind disturbance $V_{SOL} = TAS$ (TAS = true airspeed) and it can be approximately converted to CAS considering the pressure altitude (theoretically by multiplying with $\sqrt{\rho/2}$ where ρ is air density). This way the CAS is implicitly measured ($\overline{VCAS}$) which can make its estimation easier.

2.1 The implemented MMAE algorithm

For the estimation of unmeasured system parameters Multiple Model Adaptive Estimation (MMAE) is an applicable solution (see [19, 20] for example). The MMAE uses basically a set of fixed linear time invariant (LTI) models, that is designed to cover the possible parameter values. Multiple separate Kalman Filters (KF) can be designed for these LTI models characterized by distinct values of the system parameters (k_i). Each KF generates its own state estimate and output error (residual) and they have time invariant and so simple dynamics. The filters in the model-set run in parallel and at each sample time the residuals (r_i) are used to compute the conditional probability p_i for the i^{th} KF (see Figure 2.1). This gives the probability of k_i to be the actual system parameter. The overall parameter estimate is a probabilistically weighted combination of the parameters see (2.3).

Figure 2.1 shows the overall structure of multiple-model adaptive estimation (MMAE). The considered linear system models are governed by the following discrete time equations:

$$\begin{aligned} x(t+1) &= A_i x(t) + B_i u(t) + G_i w(t) \\ y(t) &= C_i x(t) + D_i u(t) + H_i v(t) \end{aligned} \tag{2.2}$$

where $x(t) \in \mathbb{R}^n$ denotes the state of the system, $u(t) \in \mathbb{R}^m$ its control input, $y(t) \in \mathbb{R}^p$ its measured noisy output, $w(t) \in \mathbb{R}^w$ the input plant disturbance that can not be measured, and $v(t) \in \mathbb{R}^v$ is the measurement noise. Vectors $w(t)$ and $v(t)$ are zero-mean white Gaussian sequences, mutually independent with covariances $E[w(t);w(\tau)] = Q_{t\tau}$ and $E[v(t);v(\tau)] = R_{t\tau}$. The initial condition $x(0)$ of (2.2) is Gaussian random vector with mean and covariance given by $E\{x(0)\} = 0$ and $E\{x(0)x^T(0)\} = P(0)$. Matrices A_i, B_i, G_i, C_i, D_i, and H_i depend on the scheduling parameters indexed by i. $G_i = I$ and $H_i = I$ are assumed in the forthcoming developments. t and $t+1$ denote consecutive discrete time steps.

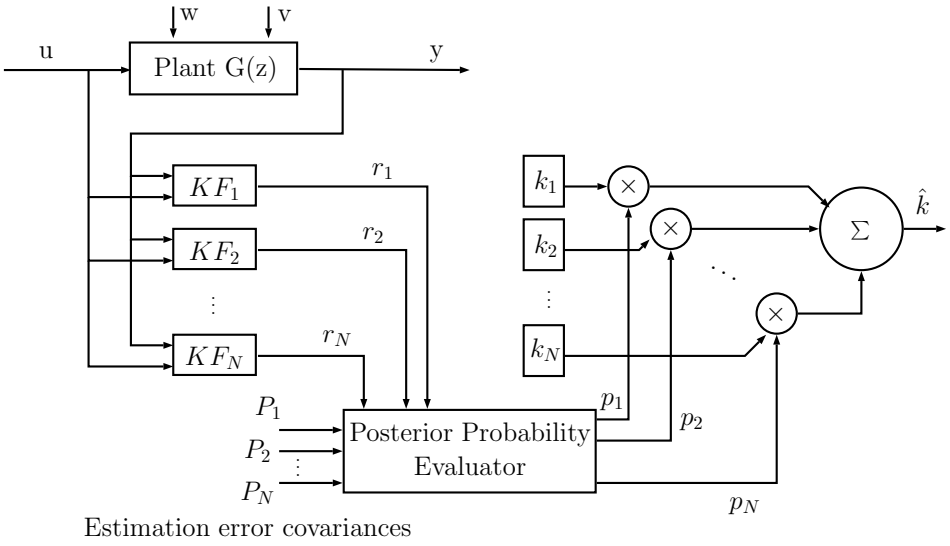

Figure 2.1: Multiple-model adaptive (parameter) estimation setup

Consider a finite set of scheduling trim parameter values $k = \{k_1, k_2, ..., k_N\}$ indexed by $i \in \{1, ...N\}$. The parameter estimate from the MMAE is given by

$$\hat{k}(t|t) := \sum_{i=1}^{N} p_i(t) k_i \tag{2.3}$$

where $\hat{k}(t|t)$ is the estimate of the parameter $k(t)$ (at time t) and $p_i(t)$ is the conditional probability that $k = k_i$, given the measurement record.

The key to the MMAE algorithm is the so-called posterior probability evaluator (PPE) which calculates, in real time, the posterior conditional probabilities $p_i(t)$; $i \in \{1, ..., N\}$. Thus, the PPE represents an identification subsystem.

The posterior probabilities can be computed on-line by the PPE using the recursive formula

$$p_i(t+1) = \frac{\beta_i e^{-E_i(t+1)}}{\sum_{j=1}^{N} p_j(t) \beta_j e^{-E_j(t+1)}} p_i(t) \tag{2.4}$$

where $p_i(0)$ are the a-priori model probabilities (initialized as $p_i(0) = 1/N$) and $E_i(t)$ and β_i are defined as

$$E_i(t) = [y(t) - \hat{y}_i(t|t-1)]^T \hat{P}_i^{-1} \underbrace{[y(t) - \hat{y}_i(t|t-1)]}_{r_i} = r_i^T \hat{P}_i^{-1} r_i \tag{2.5}$$

$$\beta_i = \frac{1}{(2\pi)^{\frac{p}{2}} \sqrt{|\hat{P}_i|}} \tag{2.6}$$

where p is the dimension of $y(t)$ and $\hat{P}_i$ is the steady state covariance matrix of residuals in i^{th} KF given by

$$\hat{P}_i = C_i P_i C_i^T + R_i \tag{2.7}$$

here P_i is the steady state estimation error covariance matrix of the i^{th} KF obtained from the related Riccati equation. PPE requires the residuals r_i calculated from the actual measured

system output $y(t)$ and the a priori output estimate $y(t|t-1)$. This requires the application of delayed KF which is summarized in the next subsection.

2.1.1 Delayed Kalman Filter

The Matlab Simulink Toolbox offers multiple built in Kalman Filter models. We decided to use the Delayed Kalman Filter model since it provided the most simple way to extract the filter residuals. The i^{th} estimator has the following state equation:

$$\begin{aligned}\hat{x}_i(t|t-1) &= A_i\hat{x}_i(t-1|t-2) + B_iu(t-1) + \\ &+ L_i\left[y(t) - C_i\hat{x}_i(t-1|t-2) - D_iu(t-1)\right]\end{aligned} \tag{2.8}$$

The delayed estimator generates output estimates $\hat{y}(t|t-1)$ and state estimates $\hat{x}(t|t-1)$ using measurements only up to $y(t)$. This particular structure is used, so that we can immediately calculate the residuals used in E_i:

$$\begin{aligned}\begin{bmatrix}\hat{y}_i(t|t-1)\\ \hat{x}_i(t|t-1)\end{bmatrix} &= \begin{bmatrix}C_i\\ I\end{bmatrix}\hat{x}_i(t|t-1) + \begin{bmatrix}D_i & 0\\ 0 & 0\end{bmatrix}\begin{bmatrix}u(t)\\ y(t)\end{bmatrix}\\ r_i &= y(t) - \hat{y}_i(t|t-1)\end{aligned} \tag{2.9}$$

2.1.2 Implementation issues

The KF bank is designed for linearized models of the aircraft which means that the inputs and outputs of the nonlinear system should be corrected with the trim point values before connecting them to the filters. However, this correction can be done only with the trim point inputs and outputs of the KF models irrespective of the actual operating point of the system. So, in the general case the nonlinear system can be considered as working around a trim point $x_0,\ u_0,\ y_0$ with linearized model $G_0 = (A_0, B_0, C_0, D_0)$ while the filters in the KF bank are running around trim points $x_{0_i},\ u_{0_i},\ y_{0_i}$ with linearized models $G_i = (A_i, B_i, C_i, D_i)$. This is shown in Figure 2.2 together with the nonlinear system.

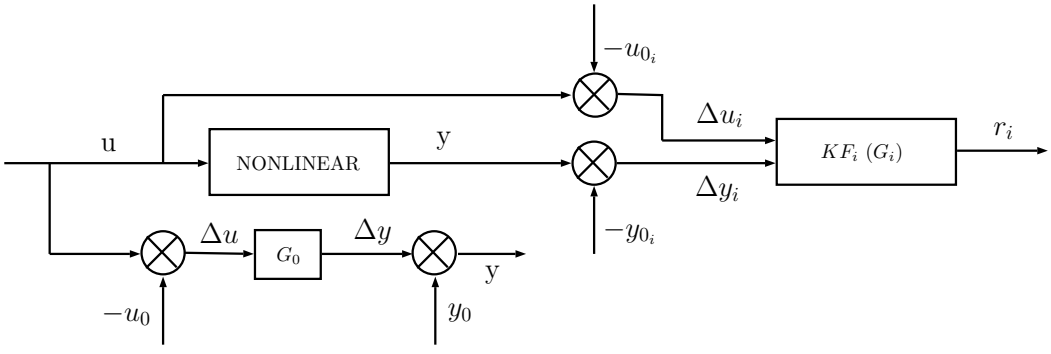

Figure 2.2: Real, virtual and KF systems

In the Figure G_0 is only a fictitious system which is the linearized system model closest to the actual operating point of the nonlinear system. In the real implementation only the KF_i filters are present as Figure 2.1 shows.

2.1.3 Dynamics of filter residuals

It is theoretically possible that all the KFs converge and give small residuals. As it will be pointed out later, this can seriously influence the estimation quality. This makes important to formally examine the most critical residual values.

Because the dynamics of G_0 and G_i should be different, since they are not linearized at the same operating point, the most critical residual could occur when both G_0 and KF_i are in steady state. Assume that the nonlinear system is in steady state such that $y = y_0$ and $u = u_0$. This case the filters are driven by $\Delta u_i = u_0 - u_{0_i}$ and $\Delta y_i = y_0 - y_{0_i}$ constant inputs. The steady state residual can be derived considering filter dynamics from (2.8) (the Δ notations are neglected as also in (2.8)) and neglecting the noise effects:

$$\begin{aligned}
&\hat{x}_i(\infty) = A_i\hat{x}_i(\infty) + B_i(u_0 - u_{0_i}) + L_i\left[y_0 - y_{0_i} - C_i\hat{x}_i(\infty) - D_i(u_0 - u_{0_i})\right] = \\
&= (A_i - L_iC_i)\hat{x}_i(\infty) + B_i(u_0 - u_{0_i}) + L_i(y_0 - y_{0_i}) - L_iD_i(u_0 - u_{0_i}) \quad \Rightarrow \\
&\hat{x}_i(\infty) = \left[I - A_i + L_iC_i)\right]^{-1}\left[B_i(u_0 - u_{0_i}) + L_i(y_0 - y_{0_i}) - L_iD_i(u_0 - u_{0_i})\right] \\
&\hat{y}_i(\infty) = C_i\hat{x}_i(\infty) + D_i(u_0 - u_{0_i}) = \\
&= C_i\left[I - A_i + L_iC_i)\right]^{-1}\left[(B_i - L_iD_i)(u_0 - u_{0_i}) + L_i(y_0 - y_{0_i})\right] + D_i(u_0 - u_{0_i})
\end{aligned} \tag{2.10}$$

Substituting the steady state filter output into the residual one gets:

$$\begin{aligned}
&r_i(\infty) = \Delta y_i - \hat{y}_i(\infty) = y_0 - y_{0_i} - \hat{y}_i(\infty) = \\
&= y_0 - y_{0_i} - D_i(u_0 - u_{0_i}) - \\
&- C_i\left[I - A_i + L_iC_i)\right]^{-1}\left[(B_i - L_iD_i)(u_0 - u_{0_i}) + L_i(y_0 - y_{0_i})\right] \\
&r_i(\infty) = R_1(y_0 - y_{0_i}) + R_2(u_0 - u_{0_i})
\end{aligned} \tag{2.11}$$

(2.11) shows that the steady state residual only depends on the difference of the trim input and output values of the system in any operating point. So, choosing a system output vector that strongly depends on CAS and only weakly depends on other parameters can lead to reliable fine estimation of CAS.

(2.11) also shows that the components of $y_0 - y_{0_i}$ and $u_0 - u_{0_i}$ are generally 'mixed' through R_1 and R_2 in r_i. This means that the sensitivity of the residual components should be examined through simulations to select components which well react to CAS changes and negligibly react to changes of other parameters. Considering (2.5) shows that another cross coupling is established between the residual components through $\hat{P}_i^{-1}$. However, diagonalizing $\hat{P}_i$ can solve this issue. This requires it to be diagonally dominant.

In the future development assume that there are residual components well reacting to CAS changes and $\hat{P}_i$ is diagonally dominant. This was verified considering the system models.

2.1.4 Application of MMAE

Two possible methods were examined. The first one is the original MMAE as presented in [19, 20]. The second one is a smoothed MMAE which is our development.

Original MMAE

[20] points out that from the KF bank the PPE parameter estimate converges to the parameter value closest to the parameter of the actual system model G_0. This means that for a sweep of

the system parameter (continuously changing A/C CAS) the MMAE output will be a staircase function jumping between the trim point parameter values (see Figure 2.18) for which the KFs were designed.

Smoothed MMAE

If one wants to have finer resolution in the CAS estimate some interpolation should be applied if possible. Considering (2.5) one can conclude that E_i is a quadratic form which depends on the residual values and is theoretically zero if $G_0 = G_i$, there is no system and measurement noise and the KF converged. Considering $G_0 \neq G_i$ cases the residual should increase as the difference between models (model parameters) increases and so, E_i increases quadratically. Considering the parameter values as independent variables a parabolic E_i curve should result which minimum gives the k_0 actual parameter value. This is shown in [19] p. 521 Fig. 2. This leads to the idea to fit a parabola to the points $k = \begin{bmatrix} k_1 & k_2 & \dots & k_N \end{bmatrix}$ and $E = \begin{bmatrix} E_1 & E_2 & \dots & E_N \end{bmatrix}$ and find its minimum point and so k_0. This possibly gives finer resolution for $\hat{k}$ if the parabola can be fitted well all the time. As previously mentioned this requires that the residual components are well reacting to CAS changes and $\hat{P}_i$ is diagonally dominant.

In our case the A380 model set includes five different CAS values ranging from 210 to 335 knots. This means that five KFs should be designed ($k = \begin{bmatrix} 210 & 240 & 270 & 300 & 335 \end{bmatrix}$) and so five points can be used to fit the parabola. To improve the accuracy of the estimation we supplement (extrapolate) the original five points if required depending on which is the smallest element out of the E_i. This is required because least squares optimal parabola fit can give a false minimum point (see Figures 2.3, 2.4).

These figures clearly show the problem with fitting a parabolic curve to the original five points. The loaded model's speed is either $210knots$ (Figure 2.3) or $335knots$ (Figure 2.4) and the minimum point of the parabolic curve is inaccurate as it is about $240knots$ in the first case and approximately $300knots$ in the second case despite the fact that the minimum E_i-s are at $210knots$ and $335knots$ respectively. The results with supplementation are more promising (see Figure 2.5, 2.6).

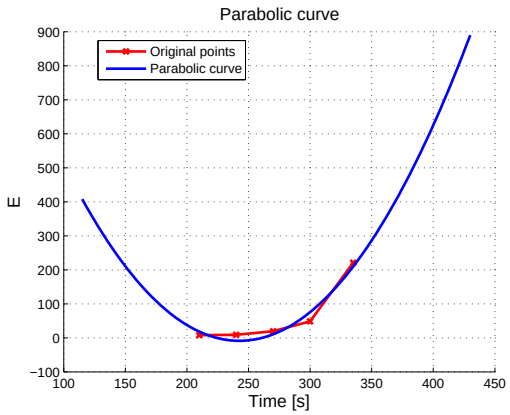

Figure 2.3: Original five points with parabolic curve to 210 knots model

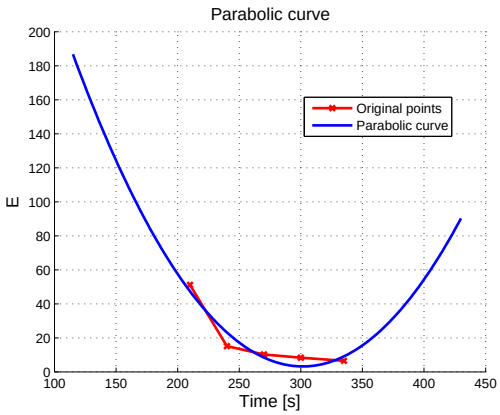

Figure 2.4: Original five points with parabolic curve to 335 knots model

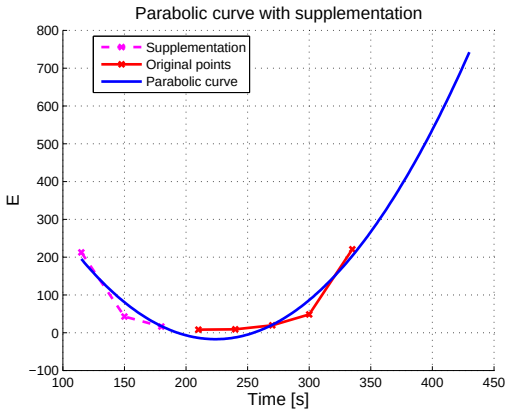

Figure 2.5: Supplemented curve to 210 knots model

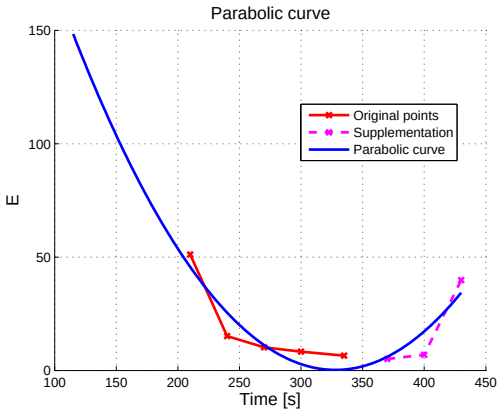

Figure 2.6: Supplemented curve to 335 knots model

In this scenario the speed estimations are closer to the model's nominal speed. Figure 2.5 shows that the estimation is approximately 224*knots* and in Figure 2.6 it is about 328*knots*. These figures clearly represent the improvement of the estimation with supplementation.

The supplementation process is explained in the following. Starting with determining the smallest E_i element out of the original five points, if the first or the second element is the smallest we supplement with three additional extrapolated values from the left, and we do the same from the right if the forth or fifth element is the smallest. The only scenario when we do not necessarily supplement the curve is when the third is the smallest value, because then the parabolic curve is sometimes adequately accurate, and so is the speed estimation, so we use a different approach in that case.

Extrapolation of the parabolic curve requires to derive a relation between given and extrapolated points. The independent coordinates are always fixed even if the k vector is extended for extrapolation. In the forthcoming formulation the independent coordinates are denoted by x and the dependent ones by y. The change of actual CAS can be imagined as the shifting of the parabola along X as it can be seen in Figure 2.7. This is the basic idea used to relate given and extrapolated points.

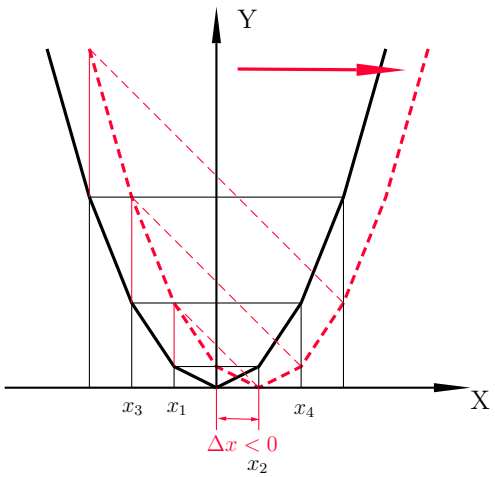

Figure 2.7: Shift of a parabola along X axis

Assume two pairs of $\{x_i,\ y_i\}$ values placed symmetrically to the minimum point $(x_1,\ y_1) \wedge (x_2,\ y_2)$ and $(x_3,\ y_3) \wedge (x_4,\ y_4)$ ($x_4 > x_2$ and $x_3 < x_1$). This means $y_1 = y_2$ and $y_3 = y_4$. Shifting the parabola by $\triangle x$ means the change of dependent points to $\{y'_i,\ x_i\}$. The base quadratic equations are

$$y_1 = a_2 x_1^2 + a_1 x_1 + a_0 \tag{2.12}$$
$$y_2 = a_2 x_2^2 + a_1 x_2 + a_0 \tag{2.13}$$

After the shift operation one gets the following:

$$y'_1 = a_2(x_1 + \triangle x)^2 + a_1(x_1 + \triangle x) + a_0 \tag{2.14}$$
$$y'_2 = a_2(x_2 + \triangle x)^2 + a_1(x_2 + \triangle x) + a_0 \tag{2.15}$$

From the previous equations we can easily calculate $\{\triangle y_1,\ \triangle y_2\}$ values

$$\triangle y_i = y'_i - y_i \tag{2.16}$$
$$\triangle y_1 = a_2 \triangle x^2 + a_1 \triangle x + 2a_2 x_1 \triangle x \tag{2.17}$$
$$\triangle y_2 = a_2 \triangle x^2 + a_1 \triangle x + 2a_2 x_2 \triangle x \tag{2.18}$$

Then we can compute the difference of $\triangle y_2$ and $\triangle y_1$

$$\triangle y_2 - \triangle y_1 = y'_2 - y'_1 = 2a_2 \triangle x(x_2 - x_1) \tag{2.19}$$

Going through the same pattern with $\{x_3,\ y_3\}, \{x_4,\ y_4\}$ pairs one gets

$$\triangle y_4 - \triangle y_3 = y'_4 - y'_3 = 2a_2 \triangle x(x_4 - x_3) \tag{2.20}$$

Collecting the derived equations

$$\begin{aligned} y'_2 - y'_1 &= 2a_2 \triangle x(x_2 - x_1) \\ y'_4 - y'_3 &= 2a_2 \triangle x(x_4 - x_3) \end{aligned} \tag{2.21}$$

it turns out that the coefficients $2a_2 \triangle x$ are the same, so the connecting lines between $y'_2,\ y'_1$ and $y'_4,\ y'_3$ are parallel. Returning back to the problem of parabola extrapolation $y'_1,\ y'_2,\ y'_3$ together with $x_1,\ x_2,\ x_3$ can be considered as the known points. The x_4 is also known from the supplementation of independent variables and y'_4 should be calculated. Obtain first the slope from the (1,2) points:

$$S = 2a_2 \triangle x = \frac{y'_2 - y'_1}{x_2 - x_1} \tag{2.22}$$

Finally, the extrapolated point results as:

$$\begin{aligned} y'_4 - y'_3 &= \frac{(y'_2 - y'_1)(x_4 - x_3)}{(x_2 - x_1)} \\ y'_4 &= y'_3 + \frac{(y'_2 - y'_1)(x_4 - x_3)}{(x_2 - x_1)} \end{aligned} \tag{2.23}$$

The steps of the procedure for parameter estimation are as follows. First the residuals from the KFs are used to compute (2.5) for each filter. Then the smallest E_i is selected

$$E_{1st} = min(E) \tag{2.24}$$

then the second smallest element E_{2nd} is also obtained. The applied equations are the following

$$S = \frac{E_{2nd} - E_{1st}}{k_{2nd} - k_{1st}} \tag{2.25}$$

where E_{1st} is the smallest element and E_{2nd} is the second smallest, while k_{1st} and k_{2nd} are the related CAS speed values respectively. Using this computed value in the next step we calculate the extrapolated values of a few or all of the remaining E elements.

$$E_j = E_i + S(k_j - k_i) \tag{2.26}$$

where E_i are the remaining elements, k_i are the related CAS speed values, and k_j are the adjusted speed values chosen from the following vector:

$$k_{l_j} = [180, 150, 115] \tag{2.27}$$

or

$$k_{h_j} = [370, 400, 430] \tag{2.28}$$

where k_l is used if the supplementation is from the left, and k_h if it is from the right and j represents the supplementary point's order.

The next case is when the third is the smallest value. In this scenario the first and the fifth value of E are compared and depending on which is smaller (2.25) is calculated where the E_{1st} will be smaller of those two. Then if the calculated result is less then $0.175(E_5 > E_1)$ or greater than $-0.175(E_1 > E_5)$ the original five points are used, otherwise the curve is supplemented from left$(E_5 > E_1)$ or right$(E_1 > E_5)$ with one additional point for the best possible parabola fit accuracy. This method and the 0.175 value is based on numerous simulation test results.

The CAS estimate is calculated as follows, given the fitted parabolic curves' quadratic equation

$$E(k) = ak^2 + bk + c \tag{2.29}$$

$$k_o = \frac{-a}{2b} \tag{2.30}$$

which is the CAS at the parabolic curve's minimum point.

In the forthcoming test campaign both the PPE-based original and the interpolated methods will be used and compared.

2.2 MMAE test campaign

The presented estimation methods were evaluated in linear and LPV simulation environments of A380 without wind disturbance.

2.2.1 Linear Simulation

The KF bank was designed for the linearized models at 20.000 ft with the following $k = \begin{bmatrix} 210 & 240 & 270 & 300 & 335 \end{bmatrix}$ parameter values. All the five systems were observable from the assumed measurements. The discrete time models were generated with 25Hz sampling. All the $\hat{P}_i$ matrices were proven to be diagonally dominant and so diagonalized by simply deleting the non-diagonal elements.

The forthcoming figures show the test results running the KF bank with one of the considered linear design models in the simplified (linear) simulation environment.

Two different reference signals were used for the simulation, the color blue indicates the first version with one doublet input (Figure 2.8) and the color magenta is the second version with three doublet inputs (Figure 2.9). The first version applies only an initial excitation meanwhile the second version continuously excites the system. The values indexed with 1 (like $Vcas1$) in the legends and shown by continuous lines use the first reference signal, and the values indexed with 3 (like $Vcas3$) and shown by dashed line, dash-dotted line or dotted line use the second reference signal.

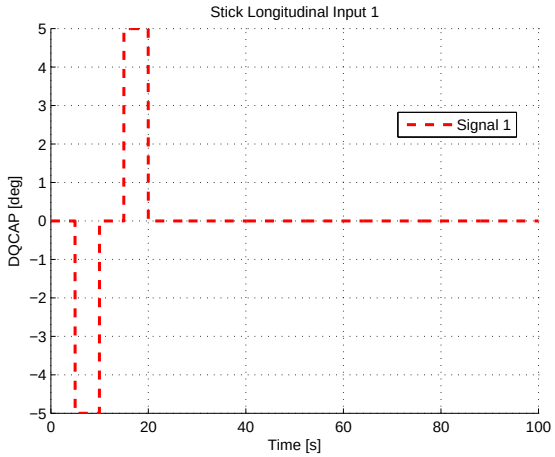

Figure 2.8: Stick Longitudinal Input 1

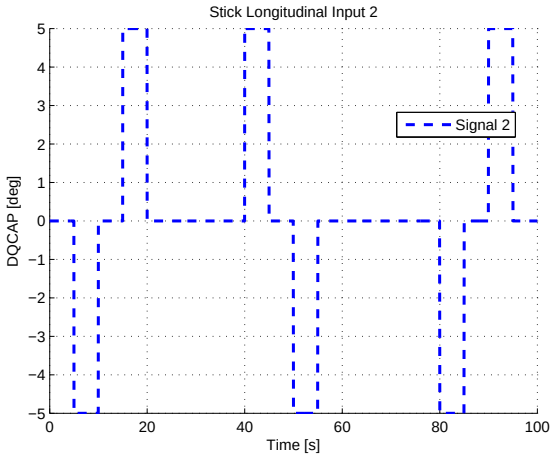

Figure 2.9: Stick Longitudinal Input 2

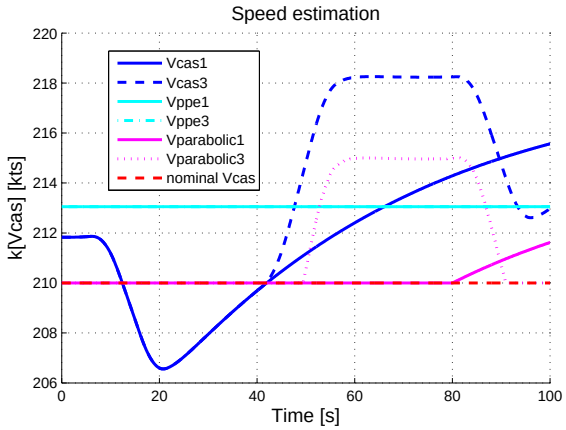

Figure 2.10: Estimation results at FL200 to 210 knots model

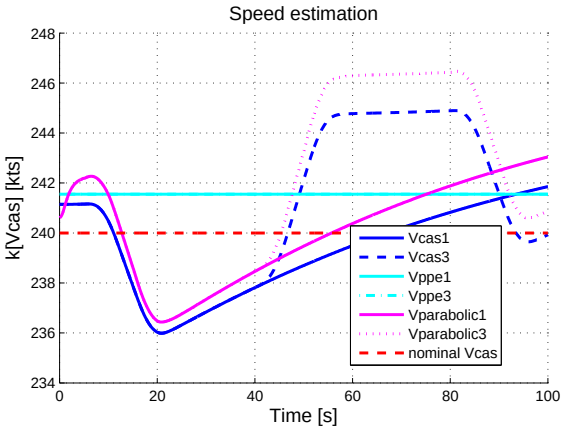

Figure 2.11: Estimation results at FL200 to 240 knots model

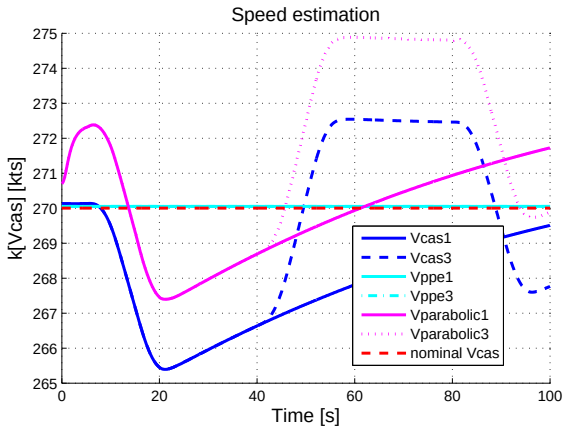

Figure 2.12: Estimation results at FL200 to 270 knots model

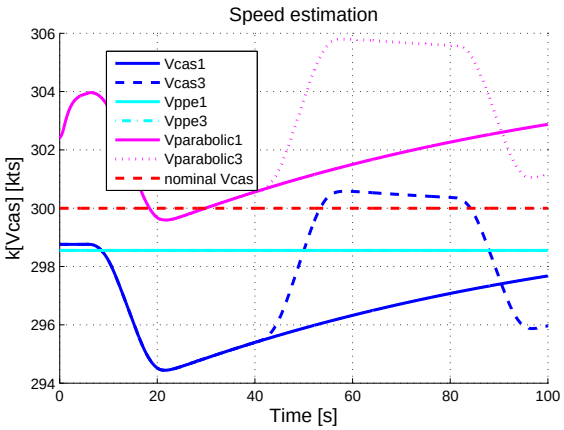

Figure 2.13: Estimation results at FL200 to 300 knots model

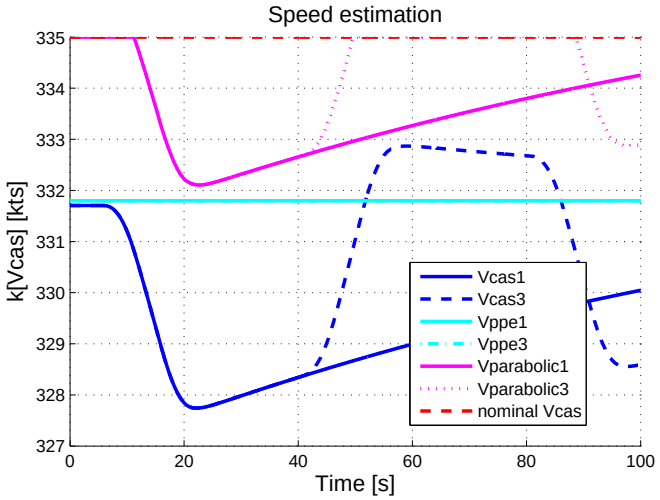

Figure 2.14: Estimation results at FL200 to 335 knots model

Below the speed of 210*knots* and above the speed of 335*knots* no values are shown because saturation was applied to filter out the speeds below or above the models limits. The PPE method's estimation (Vppe1 and Vppe3) is always constant and very close to the loaded model's nominal speed (nominal Vcas) so it is highly accurate. A deviation of less than ± 4 is observable between the two values. The parabolic method's estimation follows the calculated $Vcas$ value with adequate accuracy (around ± 5 maximum deviation) for the whole examined time interval. The different input signals cause a slight fluctuation in the speeds as the figures show, but the estimators can properly deal with this. While the PPE method can only estimate which trim speed value (previously mentioned k parameter) is the closest one to the actual speed, the parabolic method can estimate speeds in between these values.

The figures also show that the PPE does not set exactly to 210, 240 etc. slightly perturbed values are obtained instead. This is because a limitation should be applied to the posterior probability estimates $p_i(t) \geq 0.01$ to avoid zero values because the PPE can get stuck in them. This way the maximum probability results as 0.96 instead of 1 and this modifies the settled $\hat{k}$ value.

Test on linear models at different altitudes

The following table shows the test results with the linearized models for the available altitude and CAS variations at 410.000 kg mass and 43% CG position.

Table 2.1: Estimation Results

Altitude [ft]	Vcas [knots]	PPE speed [knots]	Parabolic speed [knots]
5000	210	213	210-212,5
5000	240	241,6	236-244
5000	270	270	267-272
5000	300	298,6	299-303
5000	335	331,8	332,5-334,5
12500	210	213	210-211,5
12500	240	241,5	235-243
12500	270	270	267-272
12500	300	298,6	299-304
12500	335	331	333-335
20000	210	213	210-212
20000	240	241,6	236-244
20000	270	270	267-272
20000	300	298,6	299-303
20000	335	331,8	332,5-334,5
27500	210	213	210-213
27500	240	241,6	239-244
27500	270	270	268,5-272
27500	300	298,6	299-303
27500	335	331,8	331-333
35000	210	213	210-213
35000	240	241,5	239-244
35000	270	270	268,5-271
35000	300	298,6	297-304
35000	305	298,6	303-305

The PPE model further proves reliable as it estimates almost the same CAS speeds for all the altitudes. The parabolic method has a slight variation, but still manages to estimate the CAS speed properly with less than ± 4 margin on the different altitudes.

For further demonstration two additional Figures (2.15, 2.16) were attached at FL50 and FL350.

The estimations still remain accurate as table 2.1 and the previous two figures show, even on significantly different altitudes. This means that the whole CAS and altitude range for a given mass and CG position can be covered with only five KFs.

After testing the estimation on trim point linear models it is advisable to test it on CAS dependent LPV models to see how the estimation reacts to the change in CAS. The LPV model construction and evaluation is summarized in the next section.

2.2.2 LPV simulation

LPV model construction based-on $\nu - gap$ metric

Because a grid of linear state space models (A_i, B_i, C_i, D_i) is available for different trim CAS values the easiest way to construct the LPV model is to fit interpolating polynomials to the components of the matrices. First order polynomials were fitted and tested first. Denote the

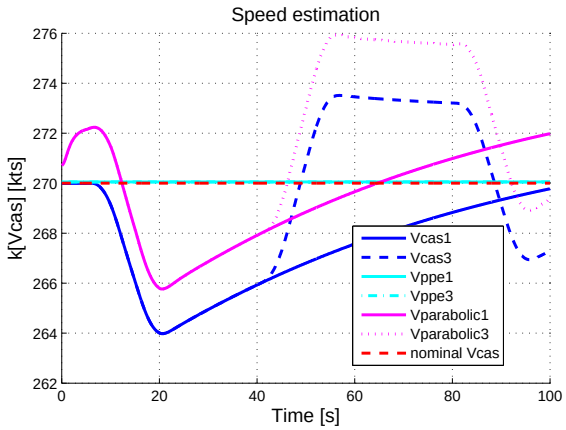

Figure 2.15: Estimation results at FL50 to 270 knots model

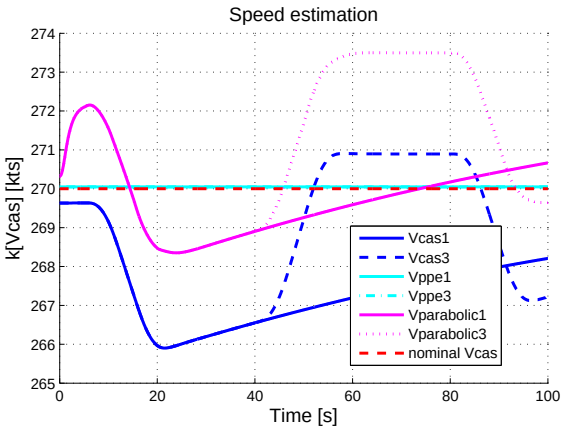

Figure 2.16: Estimation results at FL350 to 270 knots model

LPV scheduling variable by $k = CAS$ similarly to the parameters of KFs. The first order model matrices can be obtained in the following form:

$$\begin{aligned} A(k) &= A_0 + A_1 k, \quad B(k) = B_0 + B_1 k \\ C(k) &= C_0 + C_1 k, \quad D(k) = D_0 + D_1 k \end{aligned} \tag{2.31}$$

This model should be inserted into the simplified simulation where the linear model is connected to the nonlinear inputs and outputs so, trim point corrections are applied ($\Delta u = u - u_0$ and $y = \Delta y + y_0$). The best solution for LPV model insertion would be the scheduling by the actual CAS but this could lead to very complicated simulation structure. Its easier to give the scheduling variable as an additional input of the system, however this requires to schedule the u_0 and y_0 trim values also. This latter is solved by interpolating the matrices formulated from u_{0_i} and y_{0_i} column vectors:

$$\begin{aligned} U &= \begin{bmatrix} u_{0_1} & u_{0_2} & u_{0_3} & u_{0_4} & u_{0_5} \end{bmatrix} \\ Y &= \begin{bmatrix} y_{0_1} & y_{0_2} & y_{0_3} & y_{0_4} & y_{0_5} \end{bmatrix} \end{aligned} \tag{2.32}$$

The overall structure of LPV model insertion is shown in figure 2.17.

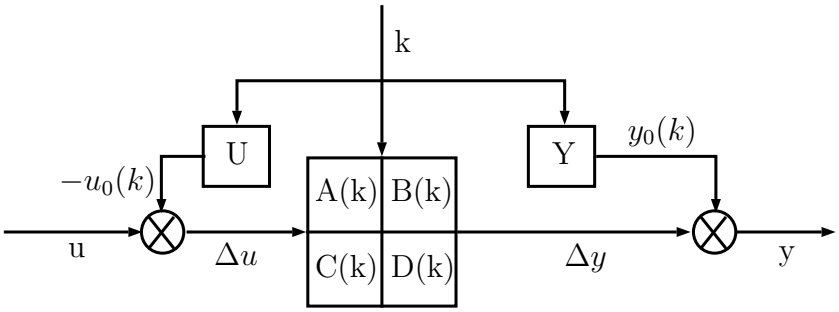

Figure 2.17: Simulation of LPV model

Simulating the controlled LPV model together with MMAE led to satisfactory results on 20.000 ft but the LPV system became unstable on every other altitude (5.000, 12.500, 27.500 and

35.000). This could be caused by the difference between the trim point linear models (for which the control was always stable) and the LPV model at the given trim point. The assumption was verified by simulating the trim point linear models obtained from the LPV model by trim $k_i = const$ parameter substitution (call these as frozen LPV models). The controller was again unstable with these constant linear models.

To quantitatively point out the problem $\nu - gap$ metric calculations were done between the linear and first order frozen LPV models:

$$\begin{aligned} &G_i = (A_i,\ B_i,\ C_i,\ D_i) \\ &G_{k_i} = (A_0 + A_1 k_i,\ B_0 + B_1 k_i,\ C_0 + C_1 k_i,\ D_0 + D_1 k_i) \\ &\delta_\nu(G_i, G_{k_i}) \in [0,1] \end{aligned} \tag{2.33}$$

The $\nu - gap$ metric is a good measure of robustness of a perturbed model relative to another model which is stable with a given controller. If it is close to 0 the perturbed model is also stable with the controller. On the other hand if it is close to 1 the perturbed model will be unstable. For details see [21].

In our case the $\nu - gap$ metric was below 0.5 for all models at 20.000 ft, but was 1 for all models at any other altitudes. So, first order models proved to be insufficient. Constructing second order models decreased the $\nu - gap$ below 0.1 in all cases and gave stable LPV models with the controller.

$$\begin{aligned} &A(k) = A_0 + A_1 k + A_2 k^2,\ \ B(k) = B_0 + B_1 k + B_2 k^2 \\ &C(k) = C_0 + C_1 k + C_2 k^2,\ \ D(k) = D_0 + D_1 k + D_2 k^2 \end{aligned} \tag{2.34}$$

Tests on LPV models considering different altitudes

Hereinafter calibrated airspeed estimation results are presented using the previously described LPV model. The two different stick input signals (2.8, 2.9) are used here as well, with similar notations and line styles. For all altitudes a continuously increasing speed input is used to test the estimator whether it can accurately follow it or not.

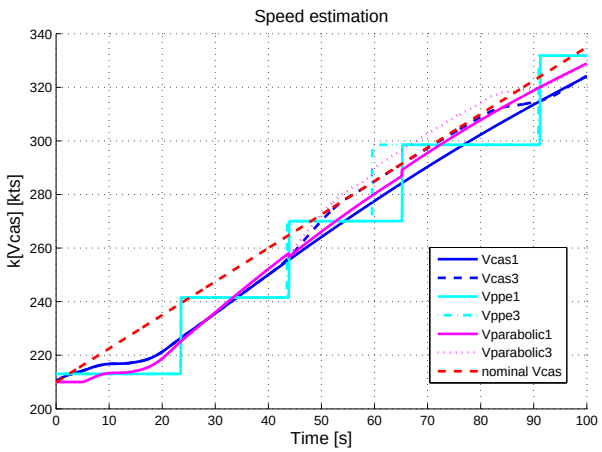

Figure 2.18: LPV model at FL50 at 210-335kts

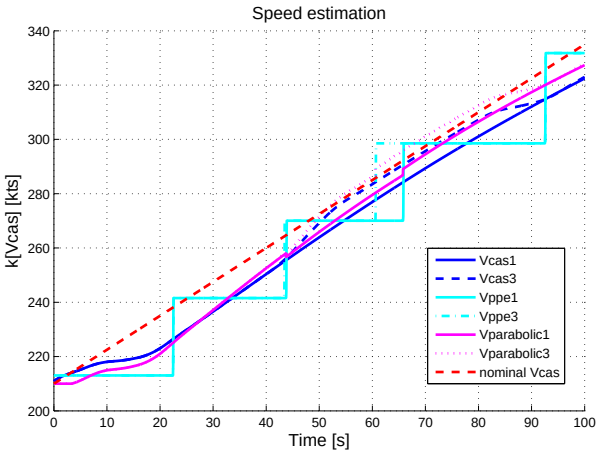

Figure 2.19: LPV model at FL125 at 210-335kts

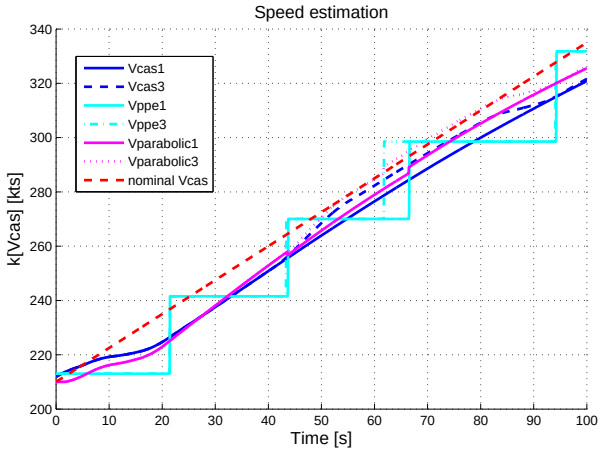

Figure 2.20: LPV model at FL200 at 210-335kts

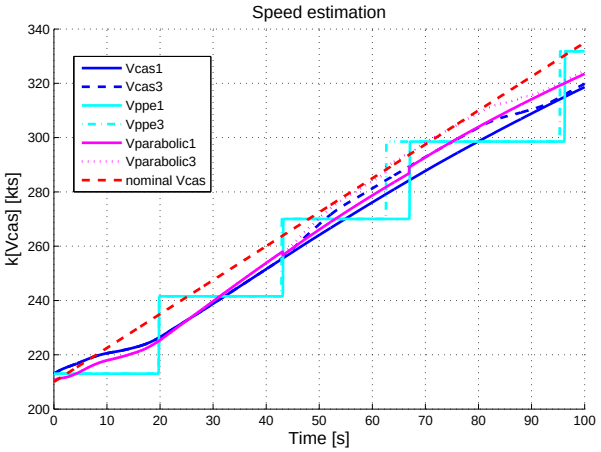

Figure 2.21: LPV model at FL275 at 210-335kts

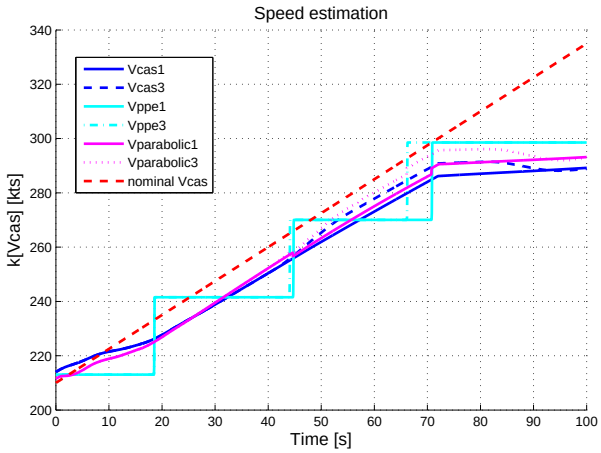

Figure 2.22: LPV model at FL350 at 210-335kts

The PPE estimator behaves as expected, it finds the parameter value nearest to the actual $Vcas$ and as it increases and gets closer to the next parameter value, the PPE jumps to the next parameter. The parabolic estimator closely follows the $Vcas$ with a usually less than $\pm 5knots$ deviation. The last Figure (2.22) might demand further explanation by the look of it, but it also behaves as expected. The last model has a maximum parameter of $305knots$ instead $335knots$. Both the PPE and the parabolic model can accurately estimate this and the PPE levels off at around $298knots$ and the parabolic approximately at $293knots$. These tests further prove the possible applicability of these methods for CAS estimation tasks.

2.3 Conclusions of Chapter 2

The developments show that the presented MMAE with parabolic interpolation and supplementation of parameter range if required can well be applied for A/C CAS estimation requiring only five parallel KFs to cover the whole altitude and CAS range at a given mass / CG configuration in the absence of wind. The proposed interpolation method greatly improved parameter estimation accuracy especially in case of continuously changing CAS parameter values (LPV simulation). The maximum parameter uncertainty (estimation error) is about $\pm 5 knots$ which can be easily compensated by a controller designed to be robust to slight scheduling parameter variations. This chapter demonstrated that the theory about using MMAE for CAS estimation with parabolic extension stands its ground, however the applied limitations such as the absence of wind places it far from reality. In the forthcoming chapter we present a more generalized solution for the problem, which is ready to be applied onboard an aircraft without further limitations.

Chapter 3

Airspeed estimation in the presence of wind

The goal of this chapter is to design an MMAE considering wind disturbances. Wind disturbance was considered as a ramp function, and it was involved to the system model as an unknown deterministic input. The wind has two longitudinal properties, magnitude (V_w), and direction (α_w). The extended model was tested in LTI, LPV and non-linear simulation environment for the Airbus A380 models.

3.1 Model modification

3.1.1 Extension of system model

The set of LTI models provided by Airbus includes wind effects both in state and output dynamics of the system. This requires state and unknown input estimation [22]. This can be represented as follows:

$$\begin{aligned} x(t+1) &= A_i x(t) + B_i u(t) + G_i d(t) + W_i w(t) \\ y(t) &= C_i x(t) + D_i u(t) + H_i d(t) + V_i v(t) \end{aligned} \tag{3.1}$$

where $d(t) \in \mathbb{R}^l$ denotes the unknown deterministic inputs (in our case wind disturbances) of the system. In the previous chapter, the following state, input and measured output values were considered in the linear model:

$$x = \begin{bmatrix} Q1 \\ VSOL \\ ASOL \\ TETA \end{bmatrix} \quad y = \begin{bmatrix} NX1 \\ NZ1 \\ Q1 \\ \overline{VCAS} \\ TETA \end{bmatrix} \quad u = \begin{bmatrix} \delta_{e(LI)} \\ \delta_{e(RI)} \\ \delta_{e(LO)} \\ \delta_{e(RO)} \\ \delta_{THS} \end{bmatrix} \tag{3.2}$$

It was considered that without wind disturbance $V_{SOL} = TAS$ (TAS = true airspeed) and it can be approximately converted to CAS considering the pressure altitude (theoretically by multiplying with $\sqrt{\rho/2}$ where ρ is air density). This was done both in the system output equation (C matrix) and y_{0_i} (see figure 2.2). This way the CAS is implicitly measured ($\overline{VCAS}$) which can make its estimation easier.

However, in case of wind disturbances the situation is not as easy, V_{SOL} should be considered different from TAS (and so CAS also) and the wind effects should be included in the disturbance vector:

$$x = \begin{bmatrix} Q1 \\ VSOL \\ ASOL \\ TETA \end{bmatrix} \quad y = \begin{bmatrix} NX1 \\ NZ1 \\ Q1 \\ VSOL \\ TETA \end{bmatrix} \quad u = \begin{bmatrix} \delta_{e(LI)} \\ \delta_{e(RI)} \\ \delta_{e(LO)} \\ \delta_{e(RO)} \\ \delta_{THS} \end{bmatrix} \quad d = \begin{bmatrix} V_w \\ \alpha_w \end{bmatrix} \tag{3.3}$$

Here, V_w is the magnitude, α_w is the direction of longitudinal wind disturbance. Considering the implementation of the KF bank it is designed for linearized models of the aircraft which means that the inputs and outputs of the nonlinear system should be corrected with the trim point values before connecting them to the filters. However, this correction can be done only with the trim point inputs and outputs of the KF models irrespective of the actual operating point of the system. So, in the general case the nonlinear system can be considered as working around a trim point $x_0,\ u_0,\ y_0$ with linearized model $G_0 = (A_0, B_0, C_0, D_0)$ while the filters in the KF bank are running around trim points $x_{0_i},\ u_{0_i},\ y_{0_i}$ with linearized models $G_i = (A_i, B_i, C_i, D_i)$. This is shown in Figure 2.2 together with the nonlinear system. In the figure G_0 is only a fictitious system which is the linearized system model closest to the actual operating point of the nonlinear system. In the real implementation only the KF_i filters are present as Figure 2.1 shows.

The application of the y_{0_i} offset correction on the output of the nonlinear system together with the transform of $VSOL$ to $\overline{VCAS}$ has led to large filter residuals if $KF_i(G_i)$ was far from the operating point G_0 of the nonlinear system in the nonwindy cases. This led to very effective estimation of the CAS as [23] summarizes.

In case of wind disturbances $VSOL = TAS + V_w$. Applying model (3.1) in the KF bank means that the estimated wind value will also include the difference between actual system TAS and the trim TAS_i value of the filter. This means that the offset effect observed in the unwindy cases will be masked and also the wind estimation results will be corrupted. Considering the estimator residuals they are usually too small to select the valid KF_i filter and so k_i parameter value. This leads to the requirement to modify the estimation strategy.

The difference between actual TAS and TAS_i of the given filter can be considered as a slowly changing offset affecting only the measured output through the H_i matrix. Introducing such an extra disturbance (d_o) leads to the following final model:

$$\begin{aligned} d &= \begin{bmatrix} V_w \\ \alpha_w \\ d_o \end{bmatrix} \\ x(t+1) &= A_i x(t) + B_i u(t) + \begin{bmatrix} G_i & 0 \end{bmatrix} d(t) + W_i w(t) \\ y(t) &= C_i x(t) + D_i u(t) + \begin{bmatrix} H_i & e_4 \end{bmatrix} d(t) + V_i v(t) \end{aligned} \tag{3.4}$$

here, e_4 is the unit vector with 1 in its fourth element. In the unwindy cases TAS to CAS transformation was applied for VSOL considering flight altitude. Here, the TAS_i values should be subtracted from VSOL as parts of y_{0_i}. However, the filters are selected based-on CAS which is altitude dependent relative to TAS. The solution is to make CAS_i to TAS_i conversion regarding the KF trim values. This can be done by the following formula:

$$TAS_i = \frac{CAS_i}{\sqrt{\rho/\rho_0}} \tag{3.5}$$

here, ρ_0 is air density at the reference altitude, while ρ is air density at actual altitude.

3.1.2 Reduction of the extended model

At first, a single state and disturbance estimator was designed for a single LTI system to test if the concept works. The time varying filter equations are as follows (estimator from [22] extended by known inputs also):

$$\begin{aligned}
&Prediction:\\
&\bar{x}_{k+1} = A_k\hat{x}_k + B_k u_k + G_k\hat{d}_k\\
&\hat{d}_{k+1} = M_{k+1}\left(y_{k+1} - C_{k+1}\bar{x}_{k+1} - D_{k+1}u_{k+1}\right)\\
&Correction:\\
&\hat{x}_{k+1} = \bar{x}_{k+1} + L_{k+1}\left(y_{k+1} - C_{k+1}\bar{x}_{k+1} - D_{k+1}u_{k+1}\right)
\end{aligned} \tag{3.6}$$

here, M_{k+1} should be designed to satisfy $M_{k+1}H_{k+1} = I$. The formulae for M, L and the error covariance prediction and correction can be found in [22]. For LTI systems the steady state M_∞ and L_∞ gains can be achieved through iteration of the estimation error covariance (Riccati equation). The steady state LTI equations result in the form:

$$\begin{aligned}
&Prediction:\\
&\bar{x}_{k+1} = A\hat{x}_k + Bu_k + G\hat{d}_k\\
&\hat{d}_{k+1} = M_\infty\left(y_{k+1} - C\bar{x}_{k+1} - Du_{k+1}\right)\\
&Correction:\\
&\hat{x}_{k+1} = \bar{x}_{k+1} + L_\infty\left(y_{k+1} - C\bar{x}_{k+1} - Du_{k+1}\right)
\end{aligned} \tag{3.7}$$

Simulations of the single LTI filter didn't give acceptable results. Examining deeper the system models showed that the effects of α_{SOL} and α_W are almost the same for all of the other states in state dynamics and for the outputs. This means that these two variables are almost undistinguishable and this could lead to poor performance. See the following four matrices for LTI model at 410 tons mass, 43% CG position, 20.000 ft altitude and 210 kts CAS. Check out the 3rd column of A together with the 2nd column of G and the 3rd column of C together with the 2nd column of H as the coefficient vectors for α_{SOL} and α_w respectively.

$$\begin{aligned}
A &= \begin{bmatrix} -0.8907 & 0.0178 & -0.4233 & 0.0000 \\ -0.0002 & -0.0077 & 0.0819 & -0.1712 \\ 0.9743 & -0.0508 & -0.4920 & -0.0000 \\ 1.0000 & 0 & 0 & 0 \end{bmatrix}\\
G &= \begin{bmatrix} -0.0178 & -0.4233 & 0 \\ 0.0077 & 0.0827 & 0 \\ 0.0509 & -0.4920 & 0 \\ 0 & 0 & 0 \end{bmatrix}
\end{aligned} \tag{3.8}$$

$$C = \begin{bmatrix} -0.0006 & -0.0004 & -0.0202 & -0.0000 \\ 0.0066 & 0.0132 & 0.1265 & 0.0000 \\ 1.0000 & 0 & 0 & 0 \\ 0 & 0.7312 & 0 & 0 \\ 0 & 0 & 0 & 1.0000 \end{bmatrix}$$
$$H = \begin{bmatrix} 0.0004 & -0.0202 & 0 \\ -0.0132 & 0.1265 & 0 \\ 0 & 0 & 0 \\ 0 & 0 & 1 \\ 0 & 0 & 0 \end{bmatrix} \tag{3.9}$$

This issue can be further evaluated by checking the observability of the system. Based on 3.1 the observability matrix can be deduced as follows.

$$\begin{aligned} x_{k+1} &= Ax_k + Gd_k \\ y_{k+1} &= Cx_{k+1} + Hd_{k+1} \\ y_{k+2} &= Cx_{k+2} + Hd_{k+2} = CAx_{k+1} + CGd_{k+1} + Hd_{k+2} \\ y_{k+3} &= Cx_{k+3} + Hd_{k+3} = CA^2x_{k+1} + CAGd_{k+1} + CGd_{k+2} + Hd_{k+3} \\ &\vdots \\ y_{k+N} &= Cx_{k+N} + Hd_{k+N} = CA^{N-1}x_{k+1} + CA^{N-2}Gd_{k+1} + CA^{N-3}Gd_{k+2} + ... + CGd_{k+N-1} + Hd_{k+N} \end{aligned} \tag{3.10}$$

Writing it in a matrix form

$$\begin{bmatrix} y_{k+1} \\ y_{k+2} \\ y_{k+3} \\ y_{k+N} \end{bmatrix} = \begin{bmatrix} C & H & & & \\ CA & CG & H & & \\ CA^2 & CAG & CG & H & \\ \vdots & \vdots & & \ddots & \\ CA^{N-1} & CA^{N-2}G & CA^{N-3}G & CG & H \end{bmatrix} \begin{bmatrix} x_{k+1} \\ d_{k+1} \\ d_{k+2} \\ d_{k+3} \\ d_{k+N} \end{bmatrix} \tag{3.11}$$

We evaluated this expression by introducing the following variables: N=4 the dimension of the state space, p=5 the number of measurements in every time step, n=4 the number of states and d=3 the number of disturbances. The system is observable when the above equation has a solution. However, adding new and new rows means an increase in the number of unknown parameters also. If the coefficient matrix has more rows than columns the equation can become solvable. This can be expressed by the following inequality:

$$Np > n + Nd \tag{3.12}$$

Considering our p=5, n=4 and d=3 parameters, $N \geq 2$ results as the minimum number of measurements. In case of N=4 the system is observable, however poorly conditioned, with a condition number $5 * 10^{10}$. If only N=2 is considered the system becomes unobservable.

Similar parameters were also found in the other LTI models. This led to system model reduction, because if one removes α_w from the disturbances its effect will still be included in the estimate of α_{SOL} by the filter. So, the final system model for filter design became:

$$\begin{aligned} d &= \begin{bmatrix} V_w \\ d_o \end{bmatrix} \\ x(t+1) &= A_i x(t) + B_i u(t) + \begin{bmatrix} G_i(:,1) & 0 \end{bmatrix} d(t) + W_i w(t) \\ y(t) &= C_i x(t) + D_i u(t) + \begin{bmatrix} H_i(:,1) & e_4 \end{bmatrix} d(t) + V_i v(t) \end{aligned} \tag{3.13}$$

here, $G_i(:,1)$ and $H_i(:,1)$ are the 1st columns of G_i and H_i respectively, where i denotes the i^{th} KF.

After removing α_w from the disturbances the observability was evaluated again. For the cases N=4 and N=2 the system was observable, and it provided much better condition numbers $5*10^5$ and $3.7*10^6$ respectively. With this system reduction the system gave acceptable results for single LTI models. As a next step a set of filters were designed for 410 tons A/C weight, 43% CG position, 20.000 ft altitude and the whole range of V_{CAS}s namely (in kts): [210 240 270 300 335].

Simulating a selected LTI model in the simplified benchmark simulation with this set of KFs gave the following results (tuning of KFs was done by trial and error simulating the corresponding LTI system model together with the filter). The estimated CAS values were calculated by subtracting the estimated wind values from the measured ground speed: $\hat{V}_{CAS}(i) = VSOL - \hat{V}_w(i)$.

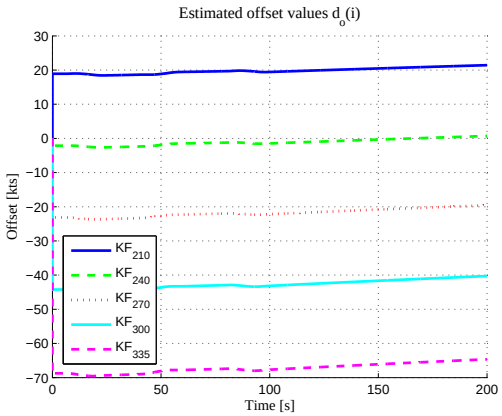

Figure 3.1: Offset estimation in LTI case (real V_{CAS}=240 kts)

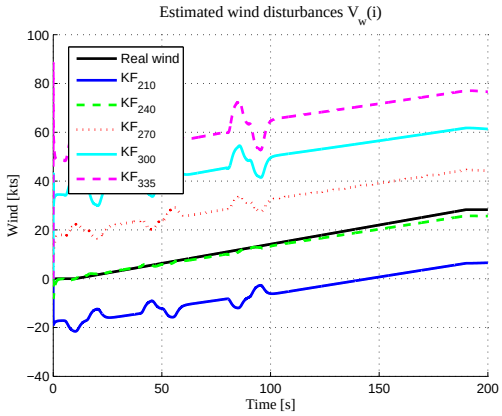

Figure 3.2: Wind estimation in LTI case (real V_{CAS}=240 kts, wind: ramp to 55 kts in 180s)

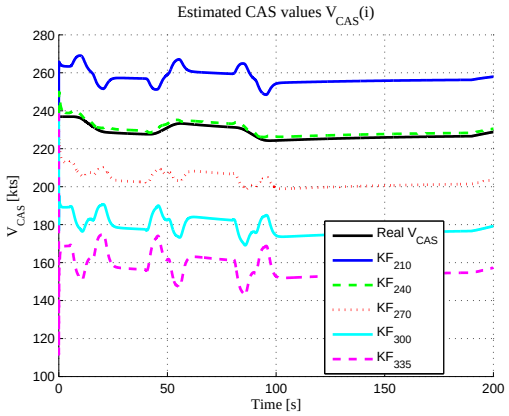

Figure 3.3: V_{CAS} estimation in LTI case

Considering these results the estimated CAS value closest to real CAS can be selected based on the estimated offset. Notice that filter offset closest to zero belongs to the best wind and so CAS estimate. A similar method as in the posterior probability estimator (PPE, see [19, 20]) can be applied. The formulae for posterior probability estimation were equation (2.3), (2.4).

Considering the estimated offset values in our case a similar exponential scaling and 'probability' calculation can be done as follows:

$$p_i(t) = \frac{e^{-K|\hat{d}_o(i,\,t)|}}{\sum_{j=1}^{N} e^{-K|\hat{d}_o(j,\,t)|}} \tag{3.14}$$

where $|\hat{d}_o(i,\,t)|$ is the absolute value of estimated offset by KF_i at time t. From this point the selection of closest estimated V_{CAS} is similar to PPE but with:

$$\hat{V}_{CAS}(t) := \sum_{i=1}^{N} p_i(t)\hat{V}_{CAS}(i,\,t) \tag{3.15}$$

$\hat{V}_{CAS}$ can also be represented as $\hat{k}$ the estimated system parameter. This representation is equivalent to the smoothed MMAE because estimated $\hat{V}_{CAS}(i,t)$ is used instead of k_i (CAS_i). These continuously varying values remove the staircase characteristics. The final block diagram summarizing the newly developed filter bank for the windy cases is shown in Figure 3.4.

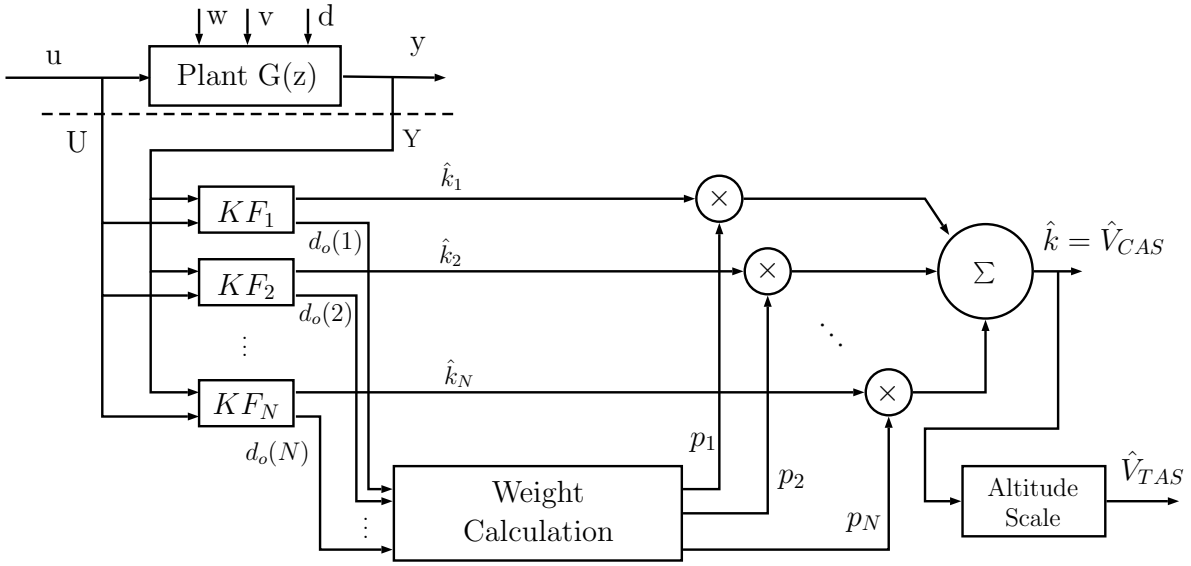

Figure 3.4: Final MMAE scheme

After completion of the design, the KF bank was tested on the five different LTI models for which it was designed to see its basic performance. Then the altitude range was extended considering the same mass and CG position in all of the cases. All of the cases were tested applying wind shear profile where wind reaching 55kts in 180s and running them until 500 seconds. This is a standard test case in Airbus simulation environment [24]. The results are summarized in table 3.1.

Table 3.1: Estimation Results for 410 tons, 43% CG (MTE = Maximum Transient Error, MEE = Maximum End Error)

Altitude [ft]	V_{CAS} [kts]	MTE [kts]	MEE [kts]
5000	210	6.5	2
5000	240	5.5	1
5000	270	4	3
5000	300	5	4
5000	335	4.5	3
12500	210	4	2
12500	240	2	3
12500	270	2	7.5
12500	300	1	6
12500	335	1	3
20000	210	2	3
20000	240	2	5
20000	270	4	6
20000	300	4	7
20000	335	2	2.5
27500	210	1	0
27500	240	3	4
27500	270	4	5.5
27500	300	6	7
27500	335	6	8
35000	210	3	3
35000	240	6	2
35000	270	12	8
35000	300	6	15
35000	305	6	18

The table shows that most of the errors are below 10kts. Because the required precision is either 20 or 10 kts (depending on the Mach number) 10 kts was decided to be the maximum allowed estimation error. Considering this the cases 35.000 ft / 270, 300, 305 kts do not satisfy the criterion. This shows that the cases at high altitude (35.000 ft) should be examined in detail.

Considering the given CAS values on an altitude the maximum is 335 kts for every altitude except for 35.000 ft. There the maximum is 300 or 305 kts. So, a large change in A/C dynamic behavior on that altitude can cause the larger estimation errors. Calculating the singular value (SVD) plots for LTI models with 410 tons, 43% CG on 20.000 ft with 300 and 335 kts and 35.000 ft with 305 kts shows significant differences as presented in Figure 3.5.

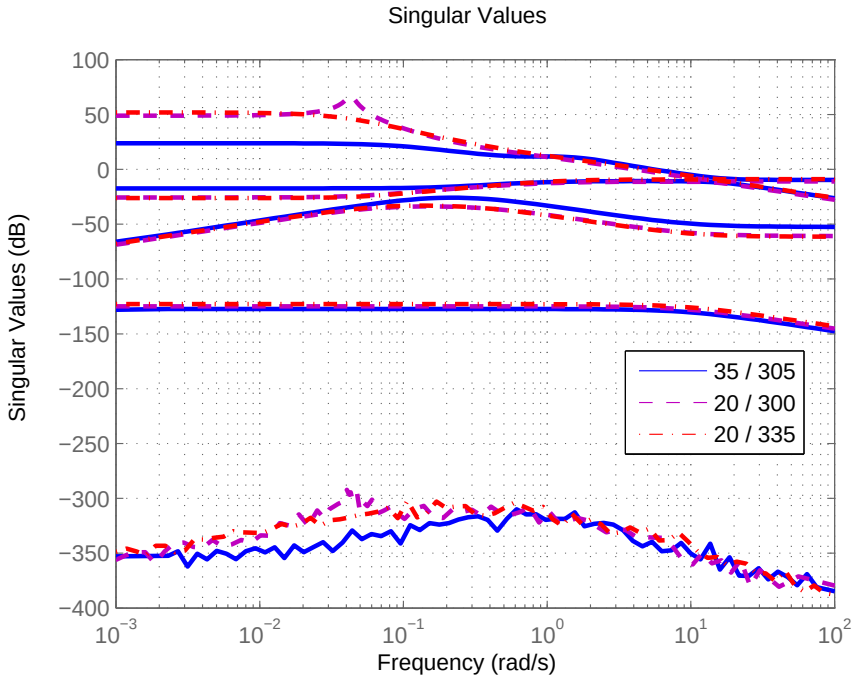

Figure 3.5: Model SVD plots (20 = 20.000 ft, 35 = 35.000 ft)

The figure shows that the largest gain for the higher altitude model is significantly smaller than for the other models. Considering the behavior of the systems the 20.000 ft / 335 kts model is closer to the 35.000 ft / 305 kts than the 20.000 ft / 300 kts one because it does not have a resonance peak. However, to select the 335 kts model instead of the 300 kts in the KF bank the estimated offset of that model should be decreased. This can be possibly done through the modification of the trim output value subtracted from system output.

With the 35.000 ft / 305 kts model the CAS is around 300 kts, so system output is around 300. However, at the KF representing the 335 kts case a TAS value proportional to 335 kts will be subtracted. This can be solved by subtracting 30 kts from the 335 kts trim value. So the trim vectors should be modified if altitude is around 35.000 ft.

Similar observations were done for flights around 270 kts at 35.000 ft. That case the 20.000 ft / 300 kts dynamics better approximated the system. This again means a required output trim point value decrease by 30 kts. So, the conversion from CAS_i trim values to TAS_i ones was modified by the subtraction of 30 kts from CAS_i before conversion if altitude is above 30.000 ft and $CAS_i > 270$ kts.

3.1.3 Aircraft weight based estimate selection

The filter bank was run for other mass and CG values of the aircraft covering again the whole altitude range. For mass 405 tons (CG 43%) the results are very similar, however, for smaller or larger mass values the results were unacceptable. This means that additional KF banks for different masses should be designed.

We introduced the structure of the linear simulation benchmark at the beginning of Chapter 2. The possible mass values published in the set of LTI models (in tons):
$\begin{bmatrix}260 & 320 & 375 & 405 & 410 & 550 & 560\end{bmatrix}$. Neglecting the very close 405 (close to 410) and 560 (close to 550) tons values, the selected masses for KF banks design are: $\begin{bmatrix}260 & 320 & 375 & 410 & 550\end{bmatrix}$. The considered CAS values in KF bank design were the given $\begin{bmatrix}210 & 240 & 270 & 300 & 335(305)\end{bmatrix}$

kts values in the database, except for the 550 tons KF bank because no 210 kts model is given for that mass. Every KF bank was designed for 20.000 ft altitude because this is the central value in the given range. For 410 tons and 550 tons only 36% CG position is available, so KF bank was designed with this value. For 320 and 375 tons only 28 %, however, for 260 tons 28, 36 and 43% are available. Design was conducted for 36% mid value in this latter case. All of the filters were tuned by trial and error.

The use of multiple KF banks means that the final estimate of CAS should be selected based-on the mass value of the aircraft. Fortunately an estimate of actual mass is also available between the measurements in case of V_{CAS} sensor errors (see [18]). The structure of the final mass dependent estimation is shown in Figure 3.6.

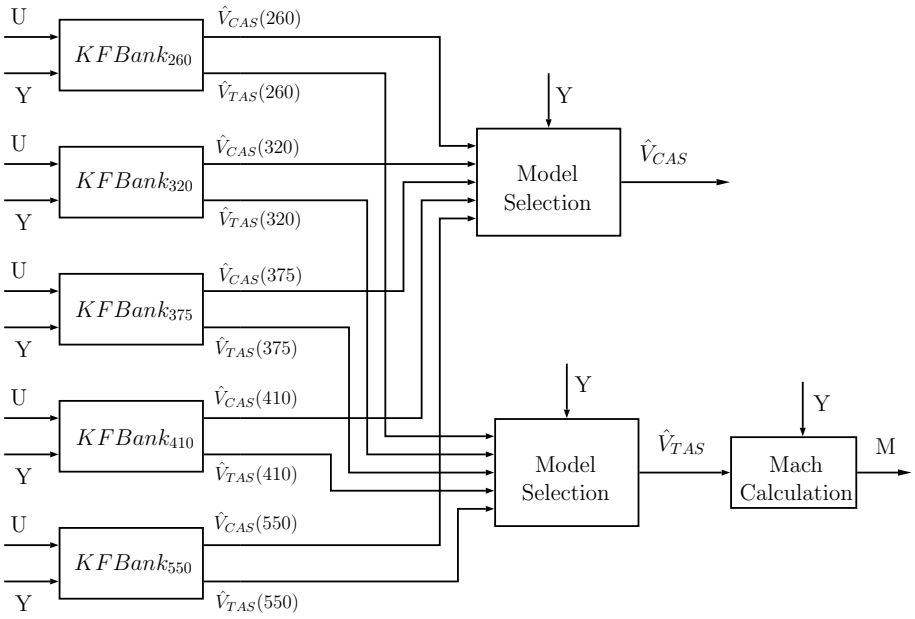

Figure 3.6: Mass dependent MMAE construction

As Figure 3.6 shows each KF bank (structure shown in Figure 3.4, $\hat{k} = \hat{V}_{CAS}(m_j)$ it can be easily converted to $\hat{V}_{TAS}(m_j)$ applying (3.5)) gives an estimate of CAS and TAS related to the given mass of the aircraft. These values should be interpolated considering A/C actual mass (m). The interpolation formula can be the following:

$$\hat{V}_{CAS} = \frac{1}{m_{j2} - m_{j1}} \left[(m_{j2} - m)\, \hat{V}_{CAS}(j1) + (m - m_{j1})\, \hat{V}_{CAS}(j2) \right] \qquad (3.16)$$
$$if \quad m_{j1} < m \leq m_{j2}$$

Of course, if the mass is smaller than the minimum value $\hat{V}_{CAS}(m_j)$ related to $min(m_j)$ is selected. A similar concept applies for masses above the maximum.

3.2 Evaluation of the V_{CAS} and mass parameterized MMAE

In the development KF banks were designed for the following mass values (tons):
$\begin{bmatrix} 260 & 320 & 375 & 410 & 550 \end{bmatrix}$. The first step of evaluation was to test the single KF banks for LTI and LPV models with given aircraft mass (covering whole available altitude and CG range)

considering a 55 kts / 180s ramp profile wind disturbance. LTI and LPV models for 405 and 560 tons were executed with the KF banks designed for 410 and 550 tons respectively. Because the length of the present work is limited, we present in more details the non-linear simulation results in Subsection 3.4.4, since they are the best representation of the real flight conditions.

3.2.1 Results with single LTI system models

The results showed that estimation performance is acceptable in most of the cases. Below 35.000 ft there are some cases with estimation errors just above 10 kts, but their number is negligible. Near 35.000 ft at and above 270 kts V_{CAS} the results improved and were satisfactory due to the before mentioned corrections.

3.2.2 Results with single LPV system models

CAS dependent LPV models were generated for all possible mass, CG and altitude values applying the method described in 2.2.2. All of them was run with the KF bank designed for the closest mass value. LPV tests again show that uncertain estimation can occur mainly on 35.000 ft, however, there are some uncertain cases on 5000 ft and 27.500 ft also. These are only critical (errors close and above 20 kts) for the 550 and 560 tons test cases. This means that for these mass values, possibly separate filter banks should be designed for every given altitude value, but this further complicates the estimation structure and is so neglected in this work.

3.2.3 Results with non-linear simulation

The provided non-linear simulation benchmark contains the effects of auto-thrust, which provides the ability of keeping a constant airspeed without the need of continuous adjustments of throttle positions by the pilots. However the linear benchmark models do not contain the effects of the auto-throttle. Because the KF banks were developed based on the linear system models, in the cases when auto-throttle was activated in the non-liner simulation environment, the results were not satisfactory. Other cases, without auto-throttle provided good airspeed estimations. In the forthcoming, only test cases where the auto-throttle is not activated are considered, and the inclusion of the throttle effects to the estimation is left for future development. This redesign only affects the system′s B and D matrices, and since they include known inputs of the system they should not affect the calculation method.

A total number of 207 non-linear simulation cases were run for evaluation. The cases contained different flight scenarios, considering various wind directions and magnitudes, several flight altitudes, and simulation lengths. Unfortunately the altitude in some simulation scenarios was above 40.000 ft, which is outside the 35.000 ft linear model range. In these cases the simulations provided less accurate results.

In general for deactivated auto-throttle scenarios the estimations were satisfactory, however for some cases we experienced divergence problems. In the forthcoming section we take a closer look on this issue, and propose a solution. The non-linear simulation results are presented in Section 3.4.4, after the correction of the mentioned convergence problem. The divergence issue can be observed on the following two figures.

Figure 3.7 shows the result for a test case where the flight altitude is 41.000 ft (outside the linear model range), the aircraft weight is 480 tons and a head wind is present.

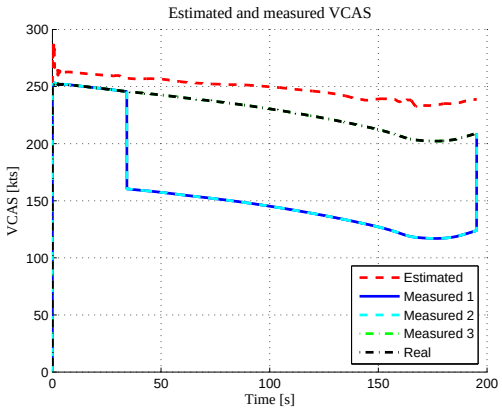

Figure 3.7: WIND-01 HEAD scenario run 7 with divergence problem

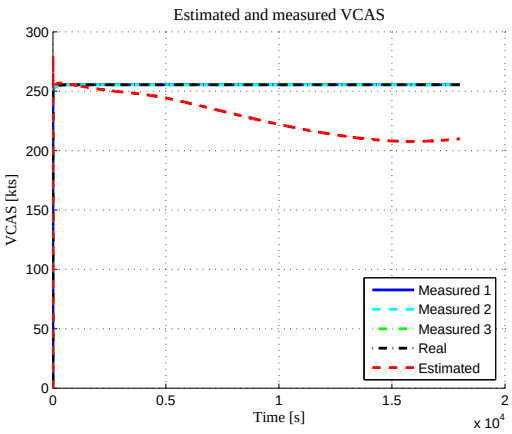

Figure 3.8: Very long flight with divergence problem

Figure 3.8 shows a test case of a very long flight simulation (20.000 seconds). The estimation diverged, and the maximum difference is reaching 50 knots what is not acceptable. Here the autopilot and auto-throttle are switched on, but switching them off did not solved the divergence problem.

3.3 Improved convergence of the algorithm

The divergence problem can be evaluated by taking a closer look on the (3.7) equations. These LTI model equations were reordered to a power series form, and an equation has been deduced for the n-th member of the series. By taking the limit of this equation if n goes to infinity, one can check the convergence of the series, which means the convergence of the filter. This can be done as it follows.

Based on (3.7) one can write

$$\begin{aligned} \hat{d}_{k+1} &= M_\infty \left(y_{k+1} - C(A\hat{x}_k + Bu_k + G\hat{d}_k) - Du_{k+1} \right) \\ \hat{x}_{k+1} &= \bar{x}_{k+1} + L_\infty \left(y_{k+1} - C\bar{x}_{k+1} - Du_{k+1} \right) \end{aligned} \tag{3.17}$$

After reordering the terms, and putting $\hat{d}_{k+1}$ and $\hat{x}_{k+1}$ to one single vector and substituting $\bar{x}_{k+1}$ also into the 2nd equation:

$$\begin{aligned} \begin{bmatrix} \hat{d}_{k+1} \\ \hat{x}_{k+1} \end{bmatrix} = \begin{bmatrix} -M_\infty CG & -M_\infty CA \\ -L_\infty CG & -L_\infty CA \end{bmatrix} \begin{bmatrix} \hat{d}_k \\ \hat{x}_k \end{bmatrix} + \begin{bmatrix} -M_\infty CB & -M_\infty D & M_\infty \\ -L_\infty CB & -L_\infty D & L_\infty \end{bmatrix} \begin{bmatrix} u_k \\ u_{k+1} \\ y_{k+1} \end{bmatrix} + \\ + \begin{bmatrix} 0 & 0 \\ G & A \end{bmatrix} \begin{bmatrix} \hat{d}_k \\ \hat{x}_k \end{bmatrix} + \begin{bmatrix} 0 & 0 & 0 \\ B & 0 & 0 \end{bmatrix} \begin{bmatrix} u_k \\ u_{k+1} \\ y_{k+1} \end{bmatrix} \end{aligned} \tag{3.18}$$

Introducing the notation:

$$
\begin{aligned}
\hat{z}_{k+1} &= \begin{bmatrix} \hat{d}_{k+1} \\ \hat{x}_{k+1} \end{bmatrix} \\
Z &= \begin{bmatrix} -M_\infty CG & -M_\infty CA \\ -L_\infty CG + G & -L_\infty CA + A \end{bmatrix} \\
V &= \begin{bmatrix} -M_\infty CB & -M_\infty D & M_\infty \\ -L_\infty CB + B & -L_\infty D & L_\infty \end{bmatrix} \\
\bar{u}_{k+1} &= \begin{bmatrix} u_k \\ u_{k+1} \\ y_{k+1} \end{bmatrix}
\end{aligned}
\tag{3.19}
$$

We can write:

$$\hat{z}_{k+1} = Z\hat{z}_k + V\bar{u}_{k+1} \tag{3.20}$$

Considering constant u and y (steady state of nonlinear system) $\bar{u}_{k+1} = u_c = const$, and the convergence evaluation showed that the z_∞ term should converge, but the simulation results were slowly drifting away from the correct values. At this point the reason was supposed to be numerical inaccuracy, and a correction was deduced. This drift can be seen in the following figure. As presented in Chapter 3.1, one of the estimated disturbances is an offset between the system's actual operating point (actual CAS), and the trim points (trim CAS values of KFs). A 30 knots offset was set for a single LTI estimator, and one can see that in 20.000s the estimation drifts away from the real value. Although this drift is small, but it is present.

Equation (3.20) can be rephrased to show the increment in every time step:

$$\hat{z}_{k+1} = \hat{z}_k + \Delta\hat{z}_{k+1} = Z\hat{z}_k + V\bar{u}_{k+1} \tag{3.21}$$

$$\Delta\hat{z}_{k+1} = Z\hat{z}_k + V\bar{u}_{k+1} - \hat{z}_k \tag{3.22}$$

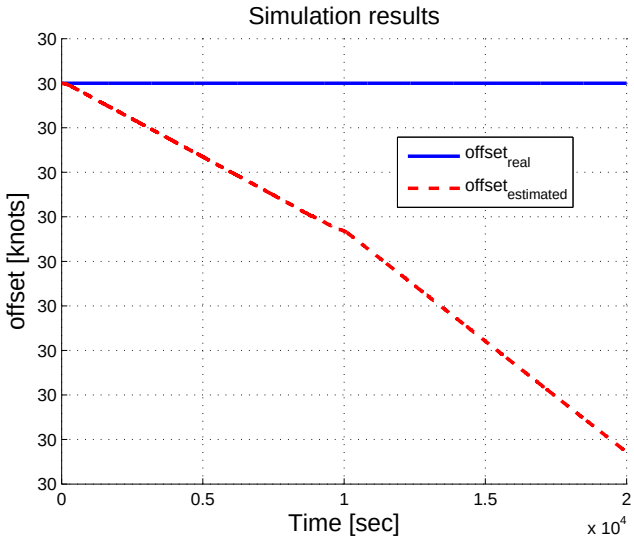

Figure 3.9: Single LTI model offset estimation in case of wind disturbance

The LTI models were modified, and the numerical accuracy of the calculation of $\Delta\hat{z}_{k+1}$ were restricted to $\varepsilon = 10^{-n}$. This means the $\hat{z}_{k+1}$ value is only updated when the Frobenius norm of

$\Delta\hat{z}_{k+1}$ was greater than the given ε. The corresponding 10^{-n} value varies for the different simulation modes, and it will be given for each simulation in the forthcoming subsections. With this modification in the case of $n = 10$ the LTI models converged, and gave a correct airspeed and offset estimation with and without wind disturbance, also for long 20.000s simulations (see Figure 3.10). Some transient oscillations are observable, but their amplitude is decreasing and completely vanish by time.

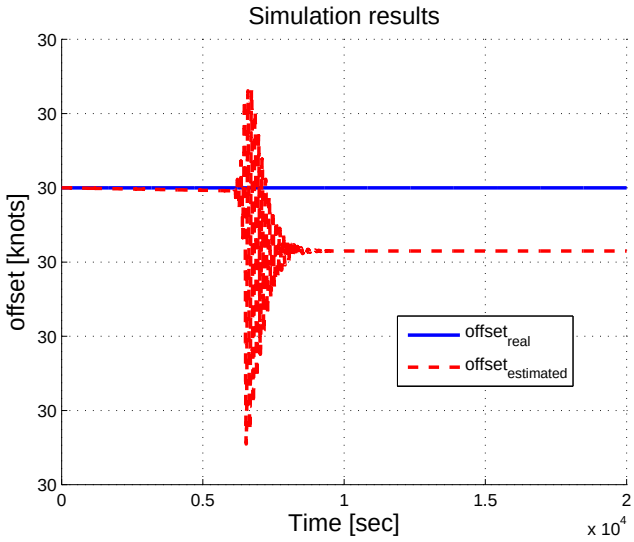

Figure 3.10: Single LTI model modified offset estimation in case of wind disturbance

As a next step the modified LTI estimator models were introduced to the original algorithm presented in Section 3.1, and for evaluation the same simulation campaign was carried out.

3.4 Evaluation of the algorithm with improved convergence

3.4.1 Linear simulation

The simulation was carried out for an LTI model of the aircraft with a given mass, which means five Kalman Filters were working parallel. The aircraft weight was 410 t and the five Kalman Filters which are estimating the disturbances were modified to take into account the numerical inaccuracy ($\varepsilon = 10^{-10}, n = 10$). The estimated CAS followed well the change in actual CAS, and converged to a constant difference between real and estimated values below the prescribed deviation limits also in very long simulations. The results were satisfactory. Figure 3.11 shows an airspeed estimation without numerical inaccuracy correction. The error between real and estimated values changes unpredictably, it can grow with time. Figure 3.12 shows the results of the corrected models for numerical inaccuracy. All other simulation parameters were unchanged. Here, the estimation error converges to a constant value.

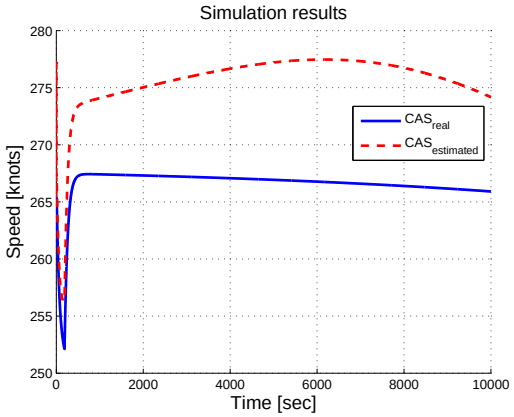

Figure 3.11: LTI model CAS estimation in case of wind disturbance without correction

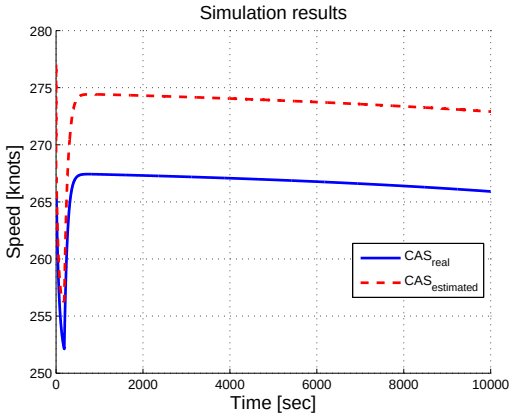

Figure 3.12: LTI model CAS estimation in case of wind disturbance with correction

3.4.2 LPV simulation

As a next step of the evaluation the proposed algorithm was tested in LPV environment. The numerical restriction had to be changed to $\varepsilon = 10^{-4}, n = 4$. Figure 3.13 shows the results for the original algorithm given in Section 3.1.3, and Figure 3.14 shows the results for the corrected algorithm. The achieved improvement is noticeable.

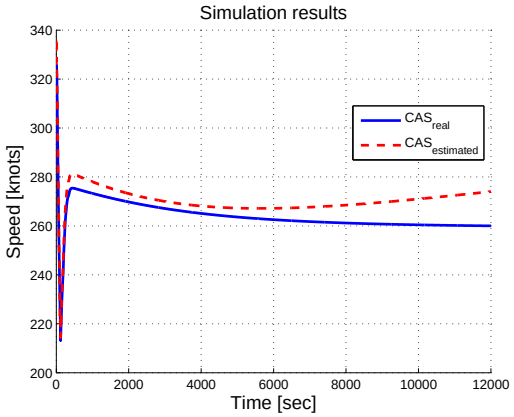

Figure 3.13: LPV model CAS estimation in case of wind disturbance without correction

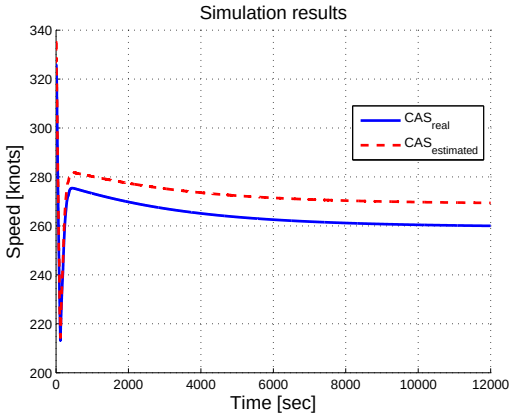

Figure 3.14: LPV model CAS estimation in case of wind disturbance with correction

3.4.3 Non-linear simulation

The final evaluation was made in the non-linear test environment provided by Airbus. The same test cases were run as in the case of the original algorithm in Section 3.2.3. The numerical restriction had to be increased to the order of $\varepsilon = 10^{-2}, n = 2$.

With the uncorrected algorithm the divergence problem was clearly observable in the very long flight simulation (see Figure 3.15). With the proposed corrected solution the divergence is completely eliminated, however some continuous 1 kts oscillations are observable (see Figure3.17). The estimation error is below 6 kts.

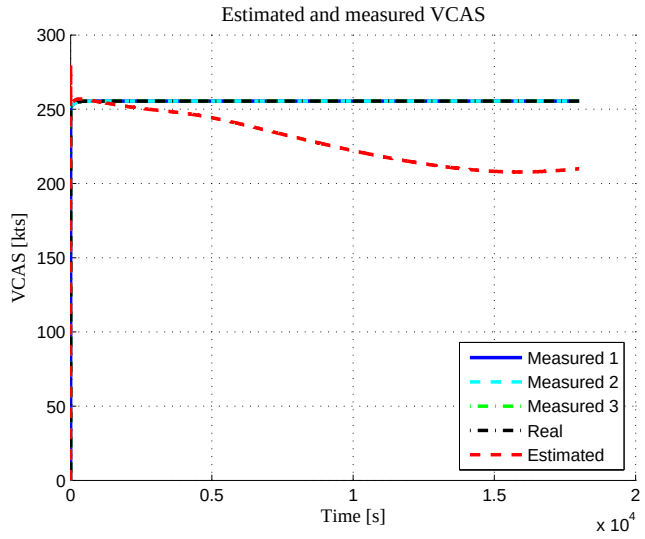

Figure 3.15: Very long flight with divergence problem

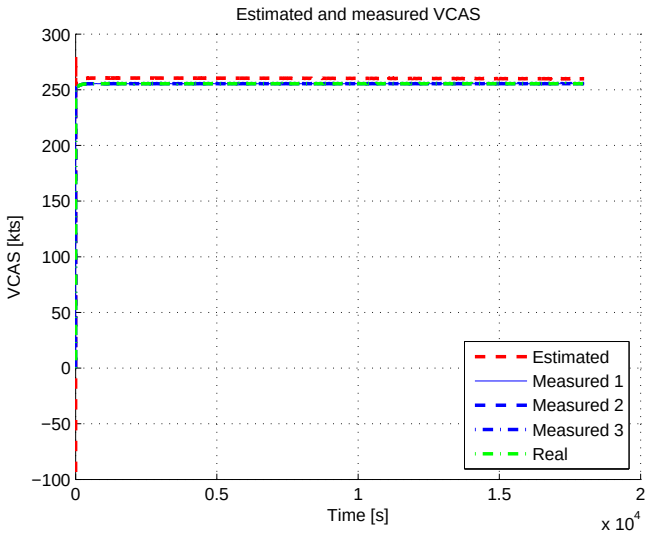

Figure 3.16: Very long flight without divergence problem

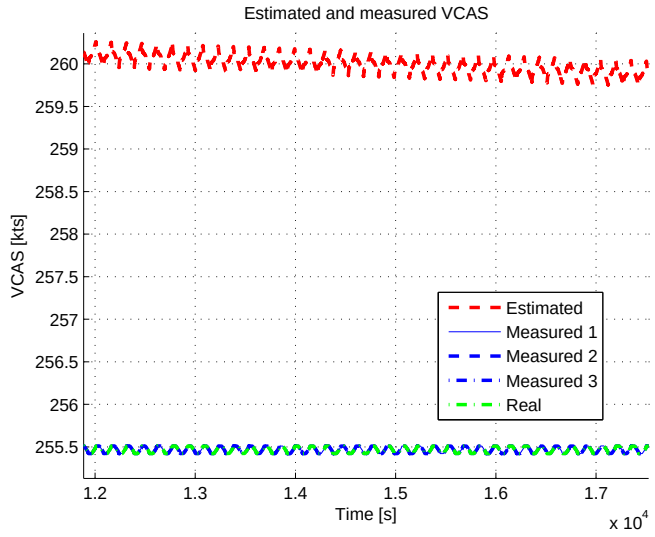

Figure 3.17: Very long flight oscillations without divergence problem

3.4.4 Non-linear simulation test campaign

In the following the detailed results of the final evaluation test campaign are presented. The cases are the official test cases provided by Airbus. Unfortunately many of them are out of the LTI model's altitude and airspeed range. In these cases the results are less accurate. This issue can be later solved by employing LTI system models considering these outside range values into the KF banks. The corresponding tables containing all simulation results can be found in the appendix.

STATIC-01

In these cases auto-thrust is not activated, flight altitude is 41.000 ft (43.000 for run 0) which is out of the range of the given LTI models (there the maximum is 35.000 ft). V_{CAS} is 250 - 270 kts which is inside the design range.

Considering estimator precision runs from 1 to 6 are excellent having maximum errors below 3 kts. In cases of 0 and 7-9 the maximum errors can be even above 20 kts, but the mean errors are all below. Run 9 is shown in Figure 3.18 with continuously decreasing estimation error after a jump at 10s.

The possible causes of worse estimations:

- In case of run 0 the mass is 375 tons which point is a design point, however, the altitude is 43.000 ft which is well above the maximum 35.000 ft.
- In cases of run 7-9 the mass is 480 tons which can not be well covered by the mass grid of the LTI models. The mass below is 410 tons, above is 550 tons (480 tons is the mid value between them). Considering the mass grid: $\begin{bmatrix}260 & 320 & 375 & 410 & 550\end{bmatrix}$ the differences between the design points are: 60, 55, 35 and 140 tons respectively. This means that there is a large step between 410 and 550 tons so, the mid value cases possibly can not be well covered by the MMAE. Additionally the altitude is 41.000 ft out of LTI model range.

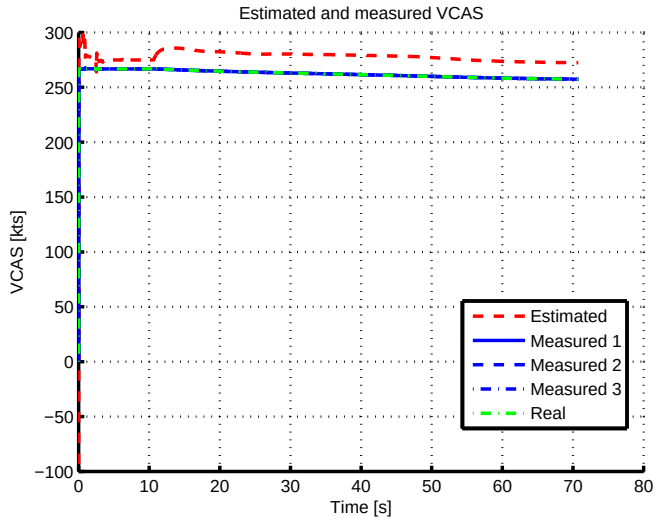

Figure 3.18: Static-01 flight run 9 scenario result

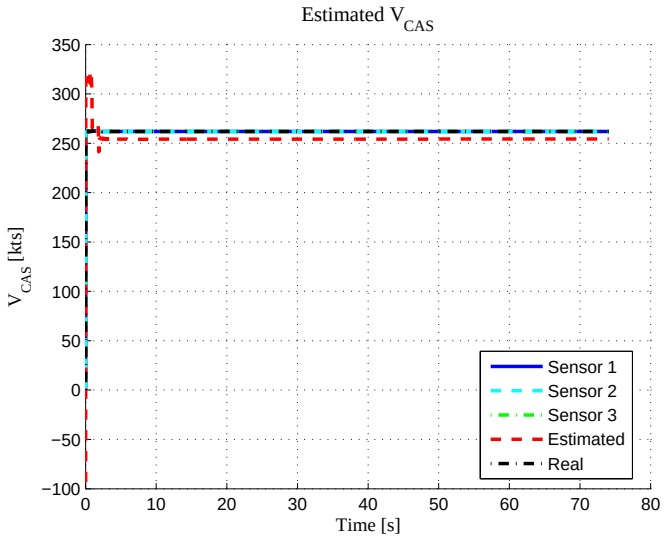

Figure 3.19: Static-01 flight run 9 on 20.000 ft flight altitude and 410 tons airplane weight

Figure 3.19 shows the result for the flight scenario STATIC-01 run 9 on a reduced flight altitude to 20.000 ft and with reduced airplane weight to 410 tons. This modification places the simulation inside the design range, and gives better results. In this case the estimation error is constant 8 kts.

STATIC-02

In these cases auto-thrust is not activated, flight altitude is 30.000 ft (inside design range). V_{CAS} is about 340 kts which is a bit outside design range. 375, 378 and 480 tons cases are run. Here, the 480 tons cases (runs 7-9) produce the best estimation statistics with maximum errors 6 kts. In the other cases the maximum estimation errors are a bit above 10 kts, but the overall estimation performance is good, with mean values below 10 kts.

STATIC-03

In these cases auto-thrust is not activated, flight altitude is 15.000 ft (inside design range). V_{CAS} is about 340 kts which is a bit outside design range. 375, 378 and 480 tons cases are run.

In these cases everything is perfect with maximum estimation errors below 5 kts. This shows that on lower altitudes the estimators work better. As an illustrative example run 2 is plotted in Figure 3.20.

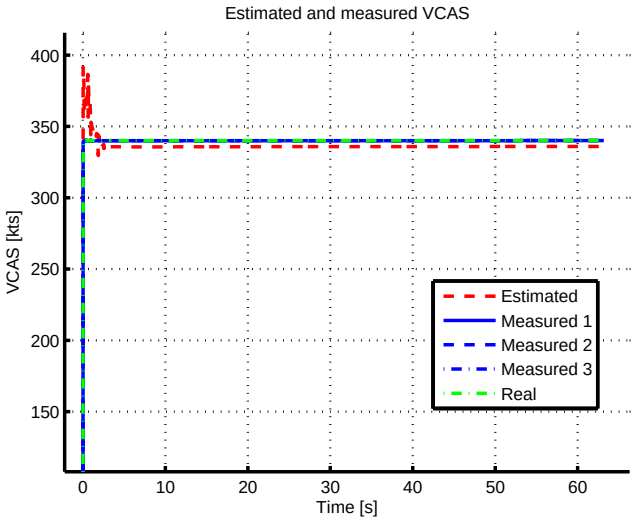

Figure 3.20: Static-03 flight run 2 scenario result

In all of the following WIND and NZLAW cases auto-thrust is activated.

WIND-01 HEAD

In these cases flight altitude is 41.000 ft outside the design range. V_{CAS} is 225 - 245 kts which is inside design range. 375, 378 and 480 tons cases are run.The 375 and 378 cases (runs 0 - 6) are acceptable with maximum errors below 10 kts, mean errors below 4 kts. However, the 480 tons cases (runs 7-9) are critical with even mean error above 14 kts (run 7 see Figure 3.21). The cause for this can be mass and altitude as in the STATIC-01 scenario.

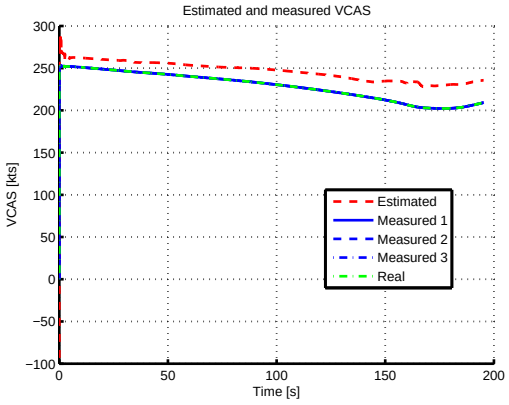

Figure 3.21: Wind-01 headwind run 7 scenario result

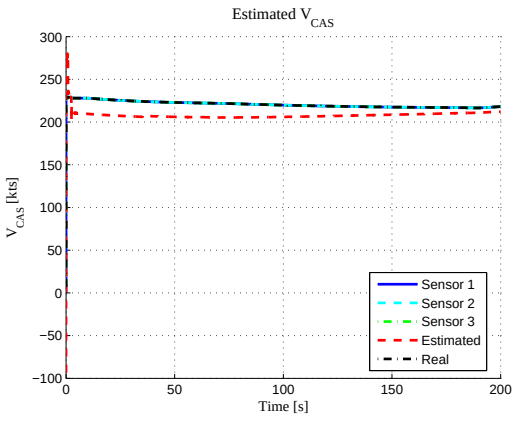

Figure 3.22: Wind-01 headwind run 7 modified altitude and mass

Figure 3.22 shows the result for the modified WIND-01 HEAD run 7 scenario. The altitude was reduced to 30.000 ft, and the aircraft mass was set to 375 tons. With these modifications

the aircraft is inside the altitude range, and close to a design weight. The result shows that the estimation error starts with a value of 18 kts, and during the simulation period it reduces to 6 kts. The result shows that, inside the altitude range better convergence can be achieved.

WIND-01 REAR

Similar altitude and mass as in the previous scenario, the average V_{CAS} is about 255 kts (inside design range). In this scenario all of the cases are unacceptable with maximum errors above 30 kts and mean errors above 13 kts. Unexpectedly the maximums are not at the beginning but several times during the run (see Figure 3.23). The cause of this unacceptable behavior is the use of auto-thrust the effect of which is not included in the MMAPE. This will be further explained at the end of the section.

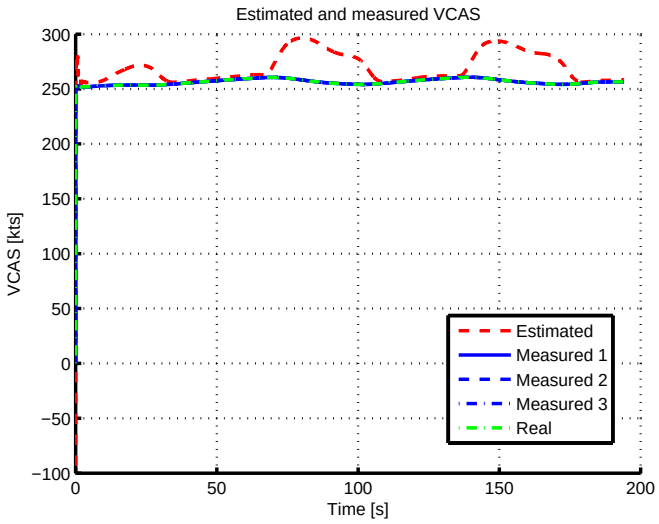

Figure 3.23: Wind-01 rear wind flight scenario run 3 result

WIND-01 SIDE

Similar test cases as in the previous scenario, but acceptable good results. Runs 0-6 are pretty nice with maximum errors below 5 kts. Runs 7-9 have maximum errors above 10 with maximum 12 kts and mean errors below 10 kts. This is the best scenario which can result from the modest use of throttle because of side (lateral) wind instead of longitudinal.

WIND-02 HEAD

In these cases flight altitude is 40.000 - 41.000 ft outside the design range. V_{CAS} is 225 - 246 kts which is inside design range. 375, 378 and 480 tons cases are run. The 375 and 378 cases (runs 0 - 6) are acceptable with maximum errors below 9 kts, mean errors below 5 kts. However, the 480 tons cases (runs 7-9) are unacceptable with errors above 30 kts (see run 9 in Figure 3.24). The cause of this can be mass and altitude as in the STATIC-01 scenario.

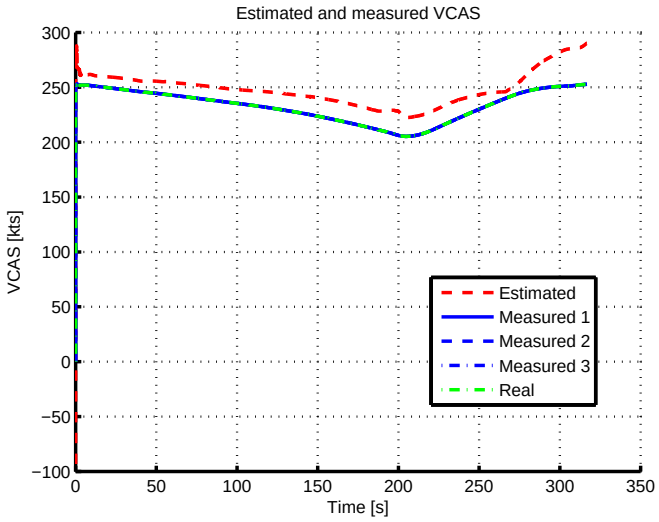

Figure 3.24: Wind-02 headwind flight scenario run 9 result

WIND-02 REAR

Similar to the WIND-01 REAR case with all results unacceptable.

WIND-02 SIDE

Similar results as in scenario WIND-01 SIDE but with larger errors (maximum errors above 20 kts, meanwhile mean errors are all below 9 kts). As a conclusion all of the cases are acceptable.

WIND-03 HEAD

Similar to the previous HEAD cases, runs 0-6 are pretty nice with maximum errors below 9 kts and mean errors below 5 kts. However runs 7-9 (480 tons cases) are unacceptable with maximum errors above 30 kts.

WIND-03 REAR

All of the runs are unacceptable as in the previous REAR cases.

WIND-03 SIDE

All of the cases are acceptable with maximum errors below 20 kts and mean errors below 12 kts.

NZLAW-07

All of the cases are unacceptable with very large estimation errors at any time. The primary cause can be the use of auto-thrust during the n_Z maneuver. Secondary causes can be the parameters of the selected test cases:

- Runs 0-9: 375, 378 and 480 tons at 43.000 ft with 245-250 kts V_{CAS}. The altitude is out of design range.
- Runs 13-24: 375, 378, 480 and 570 tons at 30.000 ft with about 335 kts V_{CAS}. 335 kts LTI models were only given at 27.500 ft altitude, at 35.000 ft 305 kts was the maximum given speed. So speed is possibly out of design range.

- Runs 25-35: 375, 378, 480 and 570 tons at 15.000 ft with about 335-340 kts V_{CAS}. The maximum given model speed was 335 kts so speed is possibly a bit out of design range.

NZLAW-08

Almost all of the results unacceptable. The primary cause can be the use of auto-thrust, the secondary cause V_{CAS} well below the 210 kts minimum V_{CAS} in LTI model set (some times the initial value is around 150 kts).

Effect of auto-thrust in the WIND scenarios

Figure 3.25 shows the simulation result for WIND-01 REAR run 4 scenario. In this case the parameters have the following values: 378.5 tons mass, 28% CG, 41.000 ft altitude, 252 kts V_{CAS} and 200 sec simulation time. The auto-thrust is activated. Then in Figure 3.26 the results are shown for the same test case, but with deactivated auto-thrust.

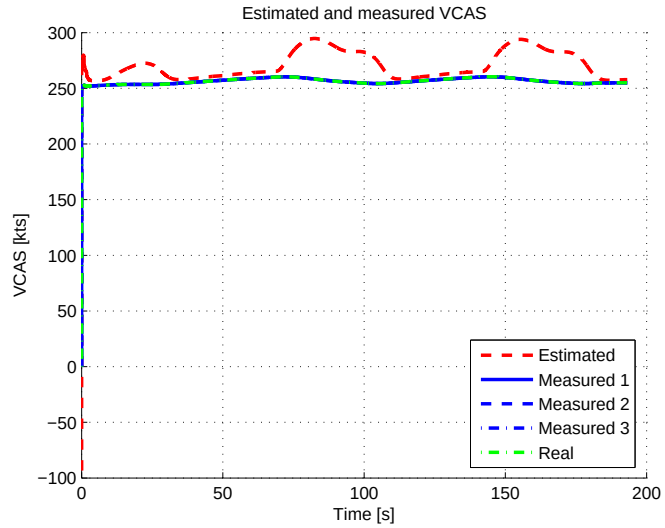

Figure 3.25: WIND-01 REAR scenario run 4 with auto-thrust

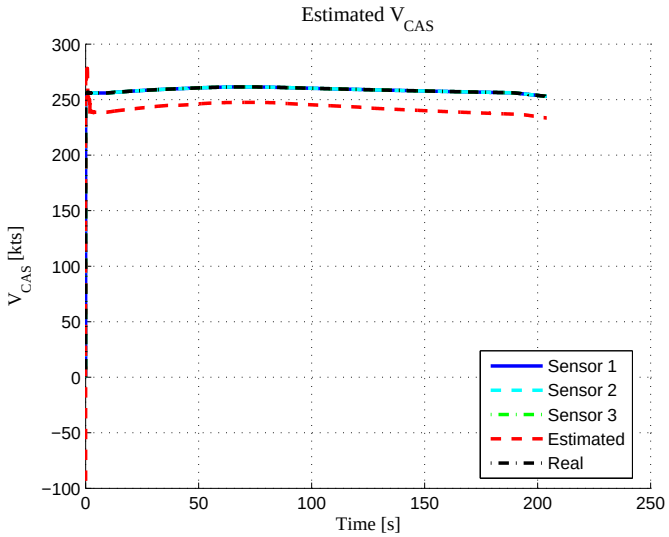

Figure 3.26: WIND-01 REAR scenario run 4 without auto-thrust

The figures show that in the non auto-thrust case the estimation has a constant deviation from the real value which is about 15 kts. In case of auto-thrust there is slow oscillation and larger (25-35 kts) differences from real value. This shows that neglecting throttle effects from the estimator design model caused significant additional estimation errors.

In this chapter we introduced the effect of wind disturbance to the estimation procedure. In order to cover the whole flight envelope of the A380 we had to design 5 KF banks based on 5 different weight values of the airplane. The final CAS estimation value is a weighted selection from the estimates of these KF banks. To achieve better convergence in long term flights we suppressed numerical calculation errors. The non-linear simulation results proved that the developed algorithm is able to provide airspeed information with adequate accuracy, however the algorithm does not contain the auto-thrust effect. The inclusion of auto-thrust to the estimation process is left for future development.

Chapter 4

Conclusions and possible future developments

The correct measurement of airspeed (calibrated airspeed CAS) is crucial to achieve safe flight conditions. Unfortunately numerous accidents happened in the aviation history due to corrupted airspeed information. At first, we have presented an overview of some representative accidents. Then the goal of this work was to present a possible airspeed estimation method based-on other sensor measurements, which can be used as a backup when the airspeed measurement system fails. The development had two phases.

In the first part, we have collected relevant literature and evaluated the so-called Multiple Model Adaptive Estimator (MMAE) proposed therein. In this part we considered simplifying assumptions in the aircraft model like absence of wind and measurement noise, and the aircraft weight was fixed to 410 tons. These assumptions placed us further from reality, but provided a suitable framework to test the proposed algorithm. MMAE applies a bank of Kalman Filters (KFs) which are designed for linear time invariant (LTI) system models of the nonlinear system each of them linearized around a given trim parameter value. The goal of MMAE is to estimate the actual system parameter value by considering a probabilistically weighted sum of trim parameter values. The probabilistic weights are calculated based-on the residual of each KF because the KF closest to actual system parameter value gives the lowest residuals. Development results pointed out that, only a total number of 5 KFs are enough to cover the whole flight envelope of an A380 airplane at a given mass value. However, in case of continuously changing system parameter (CAS) MMAE gave only a staircase function as estimate, which in case of rare sampling of the parameter interval (as it is in this work) can lead to unacceptably large estimation errors.

Our solution to this problem is the smoothing of results considering the quadratic nature of the residual terms applied in calculations. This provided the possibility to fit a parabolic curve on the error terms and its minimum point gives a more accurate parameter estimate. This solution worked well in the middle of the parameter range, however, on the boundaries it gave unsatisfactory results.

So, we proposed curve supplementation with fictitious parameter values outside the boundaries and extrapolation of the parabolic curve. A general curve can not be extrapolated, but the parabola has special properties which makes extrapolation possible as we derived.

The smoothed MMAE (smoothed by parabola fit and supplementation) gave satisfactory results even in case of continuously changing system parameter. This way we have covered the whole altitude and *CAS* range of the A380 aircraft for a given mass value with only 5 KFs running in parallel and providing good estimates of *CAS* in the whole range. However, in real

flight scenarios the change of aircraft mass, center of gravity position and the presence of wind disturbances can not be neglected. The coverage of these effects was the goal of the second part of our work.

In the second phase we extended the model applicability by resolving the restrictions, and including the wind effects in the system models. This required the application of state and disturbance estimator KFs. Originally the wind was considered as disturbance, but later we introduced an offset which represents the difference between the system's actual operating point (actual CAS), and the trim points (trim CAS values of KFs). Since the residuals of the modified KFs were very small, we used the estimate of this offset to select the most accurate KF at each time. Instead of the trim CAS values the estimated CAS of each KF (calculated from measured ground and estimated wind speed) is considered in the weighted calculation of final estimate. This inherently solves smoothing because estimated CAS changes continuously in time. The evaluation of the algorithm showed that we have to use separate KF banks for different aircraft weight values. Finally, the proposed algorithm consists of 5 KF banks (each including 5 KFs) which are enough to cover the whole flight envelope of the Airbus A380. The algorithm was tested in LTI, LPV and nonlinear simulation environments. The results were satisfactory in short simulations, but we experienced long term divergence of the estimates.

We have examined the divergence problem in detail and it has turned out that theoretically the estimator is stable and convergent, but numerical inaccuracies has led to divergence. The introduction of numerical 'stabilization' solved this problem. State updates were only propagated if the norm of the change was above a threshold. This solution preserved good results in short time and provided long term stability.

The only problem in the final nonlinear simulation test campaign was auto-throttle intervention, which is not included in the design LTI models. This resulted in large estimation errors in some of the cases but can be easily corrected by including throttle effects in the design models. However, this is unfortunately not possible for the Airbus model set because it does not include throttle effects.

The final algorithm has been presented to Airbus, and after their evaluation it is ready to be implemented on their official test bench.

Bibliography

[1] FAR Part 23. 333 Flight Envelope. Federal Aviation Administration. Downloaded 12th October 2015. [Online]. Available: http://rgl.faa.gov/Regulatory_and_Guidance_Library/rgFAR.nsf/0/35CD5C144F144C7085256687006CE915?OpenDocument&Highlight=flight%20envelope

[2] D. G. Hull, *Fundamentals of Airplane Flight Mechanics*. Springer, 2007.

[3] A. M. Schools. Pitot Tube Replacement. Donwloaded 12th October 2015. [Online]. Available: http://aircraftmechanicschools.org/pitot-tube-replacement-1078/

[4] Airspeed Definition. International Virtual Aviation Organisation. Downloaded 12th October 2015. [Online]. Available: https://www.ivao.aero/training/documentation/books/PP_ADC_airspeed.pdf

[5] Austral Lineas Aereas Flight 2553. Aviation Safety Network. Downloaded 12th October 2015. [Online]. Available: http://aviation-safety.net/database/record.php?id=19971010-0

[6] Aeroperu Flight 603. Aviation Safety Network. Downloaded 12 October 2015. [Online]. Available: http://aviation-safety.net/database/record.php?id=19961002-0

[7] Birgenair Flight 301. Aviation Safety Network. Downloaded 12 October 2015. [Online]. Available: http://aviation-safety.net/database/record.php?id=19960206-0

[8] Antonov An-148 crash. Aviation Safety Network. Downloaded 12 October 2015. [Online]. Available: http://aviation-safety.net/database/record.php?id=20110305-0

[9] Air France Flight 447. Aviation Safety Network. Downloaded 12 October 2015. [Online]. Available: http://aviation-safety.net/database/record.php?id=20090601-0

[10] (2011, February) More Pitot Tube Incidents Revealed. Aviation Today. Downloaded 12 October 2015. [Online]. Available: http://www.aviationtoday.com/regions/sa/More-Pitot-Tube-Incidents-Revealed_72414.html

[11] Ice Blocks A330 Pitot Probes. Flight Safety Foundation. Downloaded 12th October 2015. [Online]. Available: http://flightsafety.org/aerosafety-world-magazine/september-2011/ice-blocks-A330-pitot-probes

[12] Reconfiguration of Control in Flight for Integral Global Upset Recovery (RECONFIGURE). Downloaded 12th October 2015. [Online]. Available: http://reconfigure.deimos-space.com/

[13] *A330 & A340 Flight Crew Training Manual*, 2004.

[14] (2014) Flight Control Laws. Downloaded 12th October 2015. [Online]. Available: http://www.skybrary.aero/index.php/Flight_Control_Laws

[15] Airbus A380. Wikipedia. Downloaded 12th October 2015. [Online]. Available: https://en.wikipedia.org/wiki/Airbus_A380/

[16] G. N. M. Wagner, *Airbus A380 Superjumbo of the 21st Century*.

[17] *A380 Aircraft Characteristics Airport And Maintenance Plana380*. Airbus S.A.S., 2014.

[18] J. Boada-Bauxell and P. Goupil, "Preliminary Benchmark Scenario Description," Airbus, Tech. Rep., 2014.

[19] V. Hassani, A. P. Aguiar, M. Athans, and A. M. Pascoal, "Multiple Model Adaptive Estimation and Model Identification using a Minimum Energy Criterion," in *Proc. of American Control Conference 2009*, St. Louis, MO, USA, 2009, pp. 518–523.

[20] V. Hassani, A. P. Aguiar, A. M. Pascoal, and M. Athans, "A Performance Based Model-Set Design Strategy for Multiple Model Adaptive Estimation," in *Proc. of European Control Conference 2009*, Budapest, Hungary, 2009.

[21] K. Zhou and J. C. Doyle, *Essentials of Robust Control*. Prentice Hall, New Jersey, 1998.

[22] S. Gillijns and B. D. Moor, "Unbiased minimum-variance input and state estimation for linear discrete-time systems with direct feedthrough," *Automatica*, vol. 43, pp. 934–937, 2007.

[23] B. Vanek, P. Bauer, B. Beke, T. Peni, Z. Szabo, and J. Bokor, "Preliminary Application of Estimation/Diagnosis Approaches," SZTAKI, Tech. Rep., 2015.

[24] P. Goupil and J. Boada-Bauxell, "Preliminary V&V Process & Selection Matrix," Airbus, Tech. Rep., 2015.

Appendix

Table 4.1: Estimation results Static-01 case (real V_{CAS} in autopilot)

run	mass	h	avVCAS	error slope	Max err	Min err	Mean err
-	[tons]	[ft]	[kts]	[kts/s]	[kts]	[kts]	[kts]
0	374,78	42969,30	251,79	-0,03	12,25	6,20	10,05
1	374,77	40992,37	266,08	0,01	2,82	1,58	1,84
2	374,77	40974,73	266,56	0,00	2,28	2,13	2,24
3	374,77	40990,06	266,30	0,01	1,96	1,12	1,45
4	378,27	40972,98	266,29	0,00	2,78	1,54	1,62
5	378,27	40975,90	266,57	0,00	2,91	1,98	2,49
6	378,27	40989,98	266,30	0,01	2,21	1,36	1,70
7	479,73	41101,28	259,28	-0,02	24,14	8,18	18,20
8	479,72	41130,02	258,95	-0,04	22,62	7,89	17,72
9	479,73	40985,10	262,13	0,03	19,72	7,40	15,98

Table 4.2: Estimation results Static-02 case (real V_{CAS} in autopilot)

run	mass	h	avVCAS	error slope	Max err	Min err	Mean err
-	[tons]	[ft]	[kts]	[kts/s]	[kts]	[kts]	[kts]
0	374,76	29981,18	339,79	0,10	10,75	6,37	8,00
1	374,77	29981,47	339,79	0,09	10,39	6,00	7,51
2	374,76	29981,20	339,79	0,10	10,84	6,38	8,06
3	374,77	29981,50	339,79	0,09	10,29	5,75	7,35
4	378,26	29981,47	339,79	0,09	10,92	6,52	8,15
5	378,26	29981,20	339,79	0,10	11,02	6,55	8,24
6	378,26	29981,50	339,79	0,09	10,47	5,92	7,53
7	479,71	29981,85	339,79	0,11	6,01	0,02	1,97
8	479,70	29981,58	339,79	0,11	5,23	0,00	1,96
9	479,70	29982,12	339,79	-0,01	5,64	0,35	5,30

Table 4.3: Estimation results Static-03 case (real V_{CAS} in autopilot)

run	mass	h	avVCAS	error slope	Max err	Min err	Mean err
-	[tons]	[ft]	[kts]	[kts/s]	[kts]	[kts]	[kts]
0	374,77	14990,69	339,82	0,00	4,45	4,15	4,22
1	374,77	14990,68	339,82	0,00	4,45	4,15	4,22
2	374,76	14990,33	339,81	0,00	4,38	4,13	4,19
3	374,76	14990,26	339,81	0,00	3,97	3,70	3,75
4	378,26	14990,70	339,82	0,00	4,86	4,56	4,63
5	378,26	14990,33	339,81	0,00	4,80	4,55	4,60
6	378,26	14990,26	339,81	0,00	4,38	4,11	4,17
7	479,70	14990,87	339,82	0,00	1,82	1,57	1,63
8	479,70	14990,82	339,82	0,00	1,90	1,62	1,69
9	479,70	14990,75	339,82	0,00	1,98	1,67	1,74

Table 4.4: Estimation results Wind-01 HEAD case (real V_{CAS} in autopilot)

run	mass	h	avVCAS	error slope	Max err	Min err	Mean err
-	[tons]	[ft]	[kts]	[kts/s]	[kts]	[kts]	[kts]
0	374,92	40990,36	244,56	-0,01	7,78	0,02	2,71
1	374,92	40990,40	244,73	-0,01	8,24	0,01	2,90
2	374,92	40990,90	244,96	-0,01	8,56	0,01	3,01
3	374,92	40991,26	245,28	-0,01	9,31	0,00	3,26
4	378,42	40990,16	244,18	0,00	7,28	0,00	2,20
5	378,42	40990,81	244,63	-0,01	8,08	0,02	2,64
6	378,42	40991,15	245,00	-0,01	8,88	0,01	2,85
7	479,90	40913,83	228,47	0,10	29,94	9,79	17,88
8	479,90	40970,38	229,27	0,09	28,42	9,07	16,13
9	479,90	40970,27	230,67	0,06	23,07	8,64	14,48

Table 4.5: Estimation results WIND-01 REAR case (real V_{CAS} in autopilot)

run	mass	h	avVCAS	error slope	Max err	Min err	Mean err
-	[tons]	[ft]	[kts]	[kts/s]	[kts]	[kts]	[kts]
0	374,92	40992,57	256,32	0,05	36,80	2,38	14,29
1	374,92	40992,45	256,36	0,04	36,83	1,93	13,95
2	374,92	40993,36	256,32	0,05	37,93	1,80	13,86
3	374,92	40992,76	256,41	0,04	38,37	1,00	13,21
4	378,42	40992,50	256,33	0,05	36,52	2,38	14,30
5	378,42	40993,41	256,31	0,05	37,86	1,80	13,80
6	378,42	40992,73	256,41	0,03	38,19	0,94	13,12
7	479,90	40991,25	256,11	0,04	32,45	9,79	16,90
8	479,90	40992,15	256,06	0,04	33,05	7,16	16,80
9	479,90	40993,45	256,07	0,03	33,63	6,86	16,35

Table 4.6: Estimation results WIND-01 SIDE case (real V_{CAS} in autopilot)

run	mass	h	avVCAS	error slope	Max err	Min err	Mean err
-	[tons]	[ft]	[kts]	[kts/s]	[kts]	[kts]	[kts]
0	374,92	40992,10	253,32	0,00	4,91	3,23	3,80
1	374,92	40992,01	253,60	0,00	4,48	2,77	3,51
2	374,92	40991,66	253,66	0,00	4,54	2,44	3,30
3	374,92	40991,37	254,13	0,01	3,89	1,61	2,78
4	378,42	40992,04	253,29	0,00	4,89	3,27	3,81
5	378,42	40991,72	253,62	0,00	4,49	2,46	3,29
6	378,42	40991,35	254,17	0,01	3,83	1,52	2,71
7	479,90	40991,96	249,42	-0,02	12,01	7,29	9,41
8	479,90	40991,88	250,19	-0,02	11,26	6,95	8,70
9	479,90	40992,02	250,56	-0,01	10,09	6,83	8,37

Table 4.7: Estimation results WIND-02 HEAD (real V_{CAS} in autopilot)

run	mass	h	avVCAS	error slope	Max err	Min err	Mean err
-	[tons]	[ft]	[kts]	[kts/s]	[kts]	[kts]	[kts]
0	374,95	40994,37	245,93	-0,03	7,77	0,01	4,36
1	374,95	40994,38	246,12	-0,03	8,24	0,00	4,51
2	374,95	40994,57	246,11	-0,02	8,31	0,01	4,41
3	374,95	40994,69	246,25	-0,02	8,85	0,00	4,60
4	378,45	40994,20	245,23	-0,03	7,30	0,00	3,74
5	378,45	40994,71	246,00	-0,03	8,07	0,00	4,36
6	378,45	40994,71	246,14	-0,02	8,71	0,01	4,20
7	479,94	40106,90	227,58	0,00	29,26	0,01	16,19
8	479,94	40240,95	227,53	0,00	27,76	0,00	15,13
9	479,94	40218,82	233,03	0,04	37,48	5,92	15,57

Table 4.8: Estimation results WIND-02 REAR (real V_{CAS} in autopilot)

run	mass	h	avVCAS	error slope	Max err	Min err	Mean err
-	[tons]	[ft]	[kts]	[kts/s]	[kts]	[kts]	[kts]
0	374,95	40994,64	256,66	0,01	33,15	2,04	11,97
1	374,95	40994,33	256,71	0,01	33,50	1,66	12,27
2	374,95	40994,66	256,69	0,01	34,56	1,51	12,08
3	374,95	40994,55	256,75	0,02	35,80	0,87	12,33
4	378,45	40994,63	256,66	0,01	32,85	2,05	11,89
5	378,45	40994,67	256,68	0,01	34,45	1,50	12,00
6	378,45	40994,58	256,75	0,02	35,64	0,79	12,29
7	479,94	40994,68	256,26	-0,01	28,46	3,67	13,12
8	479,94	40995,30	256,23	-0,01	29,89	5,17	13,35
9	479,94	40995,36	256,38	-0,01	30,57	5,22	13,40

Table 4.9: Estimation results WIND-02 SIDE (real V_{CAS} in autopilot)

run	mass	h	avVCAS	error slope	Max err	Min err	Mean err
-	[tons]	[ft]	[kts]	[kts/s]	[kts]	[kts]	[kts]
0	374,95	40995,17	254,09	0,00	4,87	3,26	4,02
1	374,95	40994,99	254,49	0,00	4,48	2,82	3,82
2	374,95	40994,90	254,58	0,01	4,50	2,45	3,65
3	374,95	40994,67	255,33	0,02	21,71	1,62	3,95
4	378,45	40995,15	254,03	0,00	4,85	3,30	4,01
5	378,45	40994,94	254,53	0,01	4,46	2,48	3,63
6	378,45	40994,71	255,30	0,02	21,71	1,53	4,18
7	479,94	40994,74	248,22	-0,02	11,99	5,36	8,25
8	479,94	40994,74	249,36	-0,02	11,23	5,09	7,76
9	479,94	40995,15	249,76	-0,02	10,09	4,96	7,50

Table 4.10: Estimation results WIND-03 HEAD (real V_{CAS} in autopilot)

run	mass	h	avVCAS	error slope	Max err	Min err	Mean err
-	[tons]	[ft]	[kts]	[kts/s]	[kts]	[kts]	[kts]
0	374,98	40997,50	246,66	0,00	8,09	0,01	4,67
1	374,98	40997,53	246,73	-0,01	8,42	0,00	4,64
2	374,98	40997,58	246,81	-0,01	8,22	0,00	4,56
3	374,98	40997,74	246,88	0,00	8,19	0,00	4,54
4	378,48	40997,54	246,57	-0,01	7,76	0,01	4,45
5	378,48	40997,59	246,72	-0,01	8,03	0,00	4,39
6	378,48	40997,71	246,83	-0,01	8,11	0,00	4,25
7	479,97	38351,52	238,24	-0,01	26,91	0,00	12,86
8	479,97	38134,15	238,98	0,01	32,83	0,00	13,43
9	479,97	37334,73	242,16	0,06	60,18	3,75	24,38

Table 4.11: Estimation results WIND-03 REAR (real V_{CAS} in autopilot)

run	mass	h	avVCAS	error slope	Max err	Min err	Mean err
-	[tons]	[ft]	[kts]	[kts/s]	[kts]	[kts]	[kts]
0	374,98	40997,75	256,48	-0,01	25,55	0,00	6,97
1	374,98	40997,51	256,58	0,00	26,12	0,00	7,52
2	374,98	40997,63	256,55	0,00	26,89	0,00	7,61
3	374,98	40997,90	256,54	0,00	27,90	0,39	8,53
4	378,48	40997,77	256,47	-0,01	25,30	0,00	6,89
5	378,48	40997,67	256,54	0,00	26,83	0,00	7,40
6	378,48	40997,92	256,54	0,00	27,66	0,42	8,47
7	479,97	40997,58	256,60	-0,05	20,39	0,00	8,02
8	479,97	40997,60	256,55	-0,03	17,23	0,00	5,91
9	479,97	40997,92	256,53	-0,02	21,37	0,01	5,67

Table 4.12: Estimation results WIND-03 SIDE (real V_{CAS} in autopilot)

run	mass	h	avVCAS	error slope	Max err	Min err	Mean err
-	[tons]	[ft]	[kts]	[kts/s]	[kts]	[kts]	[kts]
0	374,98	40997,84	254,93	0,00	4,78	1,91	3,85
1	374,98	40997,80	255,57	0,00	4,71	2,10	3,87
2	374,98	40997,69	255,69	0,00	4,57	2,17	3,75
3	374,98	40997,72	255,92	0,01	21,73	1,65	4,72
4	378,48	40997,83	254,84	0,00	4,76	1,84	3,81
5	378,48	40997,69	255,60	0,00	4,52	2,08	3,70
6	378,48	40997,71	255,93	0,01	21,61	1,56	4,68
7	479,97	40996,54	241,47	-0,01	11,96	4,14	6,80
8	479,97	40997,42	245,92	-0,01	11,24	1,91	5,56
9	479,97	40997,58	246,43	-0,01	10,09	1,43	5,24

Table 4.13: Estimation results NZLAW-07 case (real V_{CAS} in autopilot)

run	mass	h	avVCAS	error slope	Max err	Min err	Mean err
-	[tons]	[ft]	[kts]	[kts/s]	[kts]	[kts]	[kts]
0	374,78	42978,22	248,85	-0,03	42,50	4,99	15,11
1	374,78	42976,83	248,56	0,00	47,54	2,03	16,02
2	374,77	42967,04	248,24	-0,01	50,30	0,01	16,98
3	374,78	42948,10	248,68	-0,01	49,35	0,02	16,53
4	378,28	42976,23	248,75	-0,01	44,80	2,48	15,43
5	378,27	42966,59	248,17	-0,01	50,35	0,01	17,13
6	378,27	42945,17	248,53	-0,03	49,41	0,03	16,89
7	479,72	42975,45	244,82	-0,09	44,43	16,79	29,54
8	479,72	42975,91	245,33	-0,06	46,45	16,10	28,30
9	479,73	42964,28	245,76	-0,03	47,22	13,85	27,66
13	374,77	29989,62	336,57	0,16	49,50	0,01	15,35
14	374,77	29984,17	336,71	0,18	50,26	0,01	13,82
15	374,77	29982,74	336,80	0,22	52,09	0,01	12,55
16	378,26	29989,25	336,54	0,14	49,30	0,02	15,46
17	378,26	29984,10	336,66	0,15	49,98	0,02	14,09
18	378,26	29982,75	336,75	0,20	51,69	0,00	12,71
19	479,71	29985,23	335,80	-0,20	32,75	0,00	16,75
20	479,70	29984,75	335,79	-0,20	32,88	0,00	16,43
21	479,70	29984,39	335,82	-0,18	32,38	0,00	16,18
22	568,65	29930,65	335,31	-0,08	53,40	0,01	20,05
23	568,65	29924,87	335,42	-0,09	54,11	0,01	20,42
24	568,65	29982,90	335,44	-0,29	42,27	0,00	16,32
25	374,77	15001,02	338,30	1,23	132,63	0,00	45,31
26	374,76	14993,59	338,68	1,25	129,22	0,00	43,79
27	374,76	14989,77	338,62	1,47	127,98	0,01	46,60
28	378,26	15001,72	338,30	1,18	131,09	0,02	44,17
29	378,26	14993,77	338,68	1,25	129,88	0,00	43,75
30	378,26	14981,17	338,58	1,63	130,69	0,00	49,25
31	479,70	15006,81	338,03	1,34	132,11	0,03	47,87
32	479,70	14999,12	338,53	1,30	131,50	0,01	45,81
33	479,70	14992,32	338,67	1,25	128,90	0,01	44,02
34	568,65	15004,78	336,88	0,93	117,64	0,00	37,52
35	568,65	15001,49	337,08	0,94	117,45	0,01	36,21

Table 4.14: Estimation results NZLAW-08 case (real V_{CAS} in autopilot)

run	mass	h	avVCAS	error slope	Max err	Min err	Mean err
-	[tons]	[ft]	[kts]	[kts/s]	[kts]	[kts]	[kts]
0	374,77	29886,70	195,40	-0,72	65,97	26,51	52,76
1	374,78	42807,56	188,53	0,14	18,01	0,09	6,18
2	374,78	42802,03	185,81	0,13	23,12	0,05	10,34
3	374,78	42967,90	186,42	0,19	15,76	0,03	6,04
7	374,77	29891,31	195,24	-0,71	65,82	26,48	52,72
8	374,77	29965,13	193,22	-0,68	63,99	26,47	53,01
9	374,77	30033,48	191,25	-0,63	61,88	26,44	52,83
10	568,65	30072,90	237,56	-0,13	20,24	0,01	9,61
11	568,65	30093,02	237,32	-0,13	18,95	0,02	9,66
12	568,65	30113,59	236,97	-0,13	17,69	0,02	9,56
13	368,75	14759,53	170,36	0,00		0,00	0,00
14	374,77	14890,34	206,52	-2,04	175,96	58,83	141,57
15	374,77	14971,16	202,88	-1,95	174,71	58,32	141,17
16	568,65	14954,26	237,83	-1,11	98,68	32,41	79,49
17	568,65	14972,01	237,18	-1,10	98,80	32,40	79,60
18	568,65	14991,97	236,41	-1,09	98,98	32,39	79,65
19	374,77	7538,27	204,44	1,00	156,12	0,02	41,86
20	374,77	7508,79	205,56	1,00	155,12	0,02	41,86
21	374,77	7492,21	206,02	1,01	153,59	0,01	42,29
22	568,65	7924,18	198,34	-1,56	174,82	42,20	121,66
23	568,65	7928,04	198,07	-1,57	175,84	42,11	121,85
24	568,65	7931,77	197,76	-1,58	177,37	41,59	121,95
25	374,77	7573,85	187,00	-2,40	324,09	90,78	206,92
26	374,77	7470,25	192,25	-2,35	333,86	91,57	209,60
27	374,77	7352,19	197,21	-2,30	341,78	92,01	209,26
28	568,65	7601,68	199,56	-1,33	214,24	79,74	147,38
29	568,65	7815,44	187,24	-1,11	214,90	79,78	150,64
30	568,65	7818,75	186,98	-1,12	215,62	79,82	150,91
31	374,77	4899,58	190,40	-0,80	332,03	78,02	174,80
32	374,77	4789,45	195,54	-0,33	352,07	78,67	172,28
33	374,77	4654,46	200,59	0,11	375,27	78,94	166,70
34	568,65	4878,12	200,65	0,24	236,55	73,48	116,82
35	568,65	4868,18	200,77	0,20	239,81	72,92	115,94
36	568,65	4860,02	201,08	0,23	243,45	73,15	115,80
37	374,77	1935,90	184,86	0,32	355,93	54,08	147,44
38	374,77	1813,46	190,10	0,87	380,00	37,01	140,74
39	374,77	1653,32	196,25	1,51	395,81	10,50	130,87
40	568,65	1962,90	191,11	0,82	239,46	41,01	91,67
41	568,65	1950,50	191,75	0,89	242,56	39,24	91,06
42	568,65	1943,88	192,03	0,92	246,74	38,22	90,89
43	374,77	1005,42	179,63	0,82	357,80	39,77	136,42
44	374,76	897,49	183,42	1,31	379,60	17,72	129,66
45	374,74	840,56	178,93	1,15	393,94	26,77	131,54
46	568,65	1007,74	186,99	0,93	234,70	34,40	87,19
47	568,65	996,76	187,55	0,99	237,66	32,16	86,37
48	568,65	991,43	187,80	1,04	241,58	31,17	86,19
49	374,76	908,31	177,26	2,18	349,73	0,00	104,92
50	374,75	841,61	175,04	2,17	373,22	0,07	105,06
51	374,72	817,91	169,93	2,02	397,42	0,01	110,65
52	568,65	898,33	184,73	1,87	229,49	0,06	60,11
53	568,65	891,69	185,07	1,92	232,90	0,04	60,03
54	568,65	883,25	185,49	1,98	236,66	0,04	59,92